Growth and realization of ferroelectric-photovoltaic effect in $ZnSnS_3$ thin film for solar cell and photodetector applications

A Synopsis (Approx. 5000 words)

Submitted by

Md Mohsin

Under the supervision of

Prof. Arabinda Nayak

In partial fulfilment for the award of degree

Of

DOCTOR OF PHILOSOPHY

Department of Physics
Presidency University
Kolkata

Registration No.: R-20RS209160322
Email id: *mdmohsin.rs@presiuniv.ac.in*

Date of Registration- 02.05.2022

DECLARATION

I hereby declare that the dissertation entitled "***Growth and realization of ferroelectric-photovoltaic effect in $ZnSnS_3$ thin films for solar cell and photodetector applications***" to be submitted for the degree of Doctor of Philosophy is my original work and the dissertation has not formed the basis for the award of any degree, diploma, associateship or fellowship of similar other titles. It has not been submitted to any other University or Institution for the award of any degree or diploma.

Place: Kolkata

Date: 30.09.24

Md Mohsin

(Md Mohsin)

Forwarded by the supervisor:

30/9/24

Professor of Physics
Presidency University, Kolkata

ACKNOWLEDGEMENT

I would like to express my special thanks to my guide Prof. Arabinda Nayak for his continuous support, time and valuable advice to execute these works. I would also like to extend my gratitude to DST-SERB (India) for providing fund (File no. CRG/2019/004571). I would also like to thank our respected collaborator Prof. Satyaban Bhunia for his valuable contributions and offering instrumental facility in his laboratory. Also I like to thank Mr. Jay Sharma for his valuable co-operation. I also like to thank Department of Physics, Presidency University for providing me this opportunity. We are also thankful to Gurupada Ghorai and Prof. Pratap Kumar Sahoo, School of Physical Science, NISER for providing numerous facilities.

Table of contents

1. Introduction 5

2. Literature review 6

3. Computational method 7

4. Works to fulfil the objective 7

4.1 Growth and characteristics of $ZnSnS_3$ powder

4.1.1 Synthesis 7

4.1.2 Result and discussion 8

4.2 Growth and photovoltaic characteristics of $ZnSnS_3$ thin film

4.2.1 Synthesis 17

4.2.2 Result and discussion 17

5. Conclusion 28

6. Details of published paper and conferences attended 31

1. Introduction

In recent years, considerable research has focused on developing and designing new, highly efficient, and cost-effective photovoltaic (PV) devices as alternatives to silicon (Si)-based technologies for commercial applications across various sectors. Key challenges in PV research include reducing production costs, enhancing efficiency with simpler fabrication methods, identifying new materials with favourable properties, and creating homo-junctions to minimize recombination losses caused by lattice mismatches. Despite these efforts, Si-based optoelectronic devices continue to dominate commercial applications due to their stability in open-air environments. However, the indirect bandgap of silicon remains a significant limitation for the high performance of these devices. Besides the research on clean and sustainable energy has increasingly focused on ferroelectric photovoltaics [1-4]. These materials exhibit spontaneous electrical polarization due to the breaking of spatial inversion symmetry, making them suitable for the fabrication of solar cells and photodetectors [5]. Their unique coupling of optical properties with intrinsic polarization allows for remarkable performance, including the generation of high photovoltages (around 15 V) in materials like $BiFeO_3$ [6]. Unlike traditional semiconductor p–n junctions, this high photovoltage is attributed to the domain walls in ferroelectric materials rather than their optical energy gap [1, 5-8]. The intrinsic electrical polarization, resulting from the absence of centro-symmetry, plays a key role in separating photogenerated electron-hole pairs in these materials [8]. Consequently, photovoltaic effects can occur without the need for p–n junctions, simplifying the design of photovoltaic devices [9]. Moreover, the strong remnant polarization present in ferroelectric materials provides a driving force for the separation of photogenerated electron-hole pairs within the absorber layer, which effectively lowers charge recombination rates. In some instances, the polarizing field in ferroelectric materials can be up to an order of magnitude stronger than the built-in electric field found in conventional p–n junctions.

Since few recent years, the multiferroic material $BiFeO_3$ (BFO) has gained considerable attention for photovoltaic (PV) device applications. However, its solar cells have demonstrated a relatively low energy conversion efficiency (~0.003%), mainly due to its large optical band gap (~2.7 eV), high electrical resistivity (~10^{10} Ω-cm), and exceptionally high hole effective mass (5–10 m_e). Other ferroelectric materials, such as $LiNbO_3$, $Pb(Zr_{1-x}Ti_x)O_3$ (PZT), and BZT-BCT ($0.5Ba(Zr_{0.2}Ti_{0.8})O_3$-$0.5(Ba_{0.7}Ca_{0.3})TiO_3$), $KBiFe_2O_5$ also exhibit large band gaps (greater than 3.0 eV), limiting their absorption to the ultraviolet (UV) region of sunlight [5,10-12]. A notable advancement has been achieved with ferroelectric La-doped PZT epitaxial films, reaching a photovoltaic power conversion efficiency of approximately 0.28%, despite their large band gap energy (3.2–3.6 eV) [13]. Recently, hybrid perovskite materials based on organic groups [$CH_3NH_3PbI_3$, $CH_3NH_3PbBr_3$] have also been explored [9, 13]. Several other well-known inorganic ferroelectric materials, including $BaTiO_3$, SbI_5, $KNbO_3$, $PbTiO_3$, $Bi4Ti_3O_{12}$, and $Bi_5Ti_3FeO_{15}$, have been studied extensively over the years, both experimentally and theoretically [14-18]. However, these studies have yielded unsatisfied results, primarily due to the materials' high optical bandgaps, low electric polarization, or a combination of both. Since two key parameters for effective photovoltaic materials are the light absorption coefficient (~10^4 cm^{-1}) and carrier concentration (~10^{15} cm^{-3}), are influenced by the optical band gap, small band gap polar materials, such as ferroelectrics, have attracted significant interest in PV research [8]. Therefore, to fully harness the potential of ferroelectric photovoltaic

effects, it is essential to discover novel materials with strong electrical polarization and a band gap energy close to 1.5 eV.

A recently discovered ferroelectric material, $LiNbO_3$ (LN)-structured zinc-tin-sulphide (LN-$ZnSnS_3$), has drawn our attention due to its promising properties. This lead-free absorber offers several advantages in terms of its ferroelectric and optical characteristics, as suggested by first-principle studies [19, 20]. According to theoretical calculations, replacing oxygen with sulfur in $ZnSnO_3$ significantly reduces the bandgap from 3.0 eV to 1.3 eV, while maintaining the material's high remnant polarization (~59 μC/cm²) [19, 20]. Although $ZnSnO_3$ generates excellent photovoltage due to its strong remnant polarization, it performs poorly in absorbing the solar spectrum. The substitution of oxygen with sulphur not only improves the dielectric constant but also reduces the hole effective mass [19]. The combination of a low energy band gap of 1.3 eV, which is near the maximum efficiency predicted by the Shockley-Queisser limit, and a large remnant polarization of 59 μC/cm², makes $ZnSnS_3$ a promising material for overcoming several challenges in photovoltaic applications. Additionally, the constituent elements of this material are non-toxic and abundantly available on earth.

In the work, we utilize straightforward synthesis technique including hydrothermal and spray pyrolysis for the fabrication and demonstration of the photovoltaic effect in LN-$ZnSnS_3$ ferroelectric materials. Various characteristics and photovoltaic parameters are studied and analysed of the grown materials, intended for use in solar cells and photodetectors.

2. Literature review

The structure of $ZnSnS_3$ is trigonal $LiNbO_3$ (LN) structured having space group R3c (161). And it belongs to II-IV-VI group and constituent elements Zn, Sn and S occupy particular positions to make a ordered crystal structure. There are very few reported research article about study and research about $ZnSnS_3$.

Kolb et al. shows that $ZnSnS_3$ crystal structures can form stable configurations with promising electronic properties. The primitive cell has lattice parameters of a = b = c = 0.676 nm and angles $\alpha = \beta = \gamma = 55.79°$ [19]. $ZnSnS_3$ exhibits ferroelectric properties, with a potential spontaneous polarization of 59 μC/cm², which is advantageous for photovoltaic applications by enhancing charge separation and reducing recombination losses in solar cells. Its band gap is well-suited for solar energy absorption, with a direct bandgap of 1.3 eV, making $ZnSnS_3$ an effective absorber of visible light—critical for high-efficiency solar cells [19, 20]. The band structure of $ZnSnS_3$ is depicted in Fig.2.1. Additionally, $ZnSnS_3$ has a high dielectric constant (~10) and a low effective mass of holes (0.35 m_e) [19].

There are no practical investigations into the synthesis and characterization of $ZnSnS_3$ for photovoltaic applications. However, a few reported studies have explored $ZnSnS_3$ for energy storage, or as anode materials in sodium and lithium-ion batteries. Jia et al. experimentally investigate the application of $ZnSnS_3$ combined with reduced graphene oxide (rGO) for the application of anode material for sodium or lithium ion batteries [21]. Liu et al. synthesized hollow $ZnSnS_3$ nano-microcubes to enhance sodium ion batteries along with studing reaction kinetics, cycling stability, and rate capability of nitrogen and sulfur dual-doped reduced graphene oxide encapsulating hollow $ZnSnS_3$ nano-microcubes (N/S-rGO@) $ZnSnS_3$) [22]. Xu et al. developed composite material consisting of $ZnSnS_3$ nanodots embedded in a nitrogen-

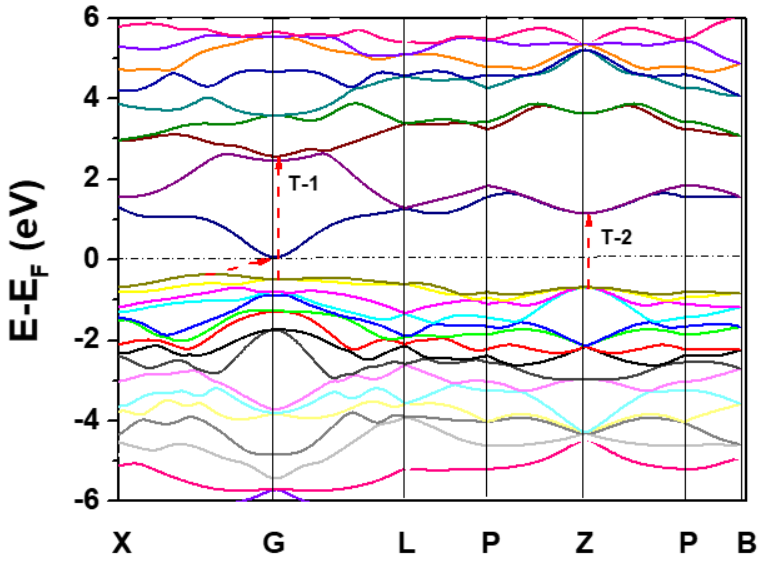

Figure 2.1 Energy band structure of $ZnSnS_3$ (Generated by Quantum espresso software)

doped graphene framework from bimetal-organic frameworks (MOFs) for the application of lithium battery energy storage and for optimizing battery performance and discover that it provide a highly tunable structure along with faster electron, ion transport and high reversible capacity [23].

3. Computational method implemented: The band structure of $ZnSnS_3$ was calculated using density functional theory (DFT) with projector-augmented wave (PAW) pseudo-potentials in Quantum Espresso (open source software). The Perdew-Burke-Ernzerhof (PBE) form of the generalized gradient approximation (GGA) was used for exchange-correlation energies. A kinetic energy cut-off of 30 Ry and charge density cut-off of 600 Ry were applied. Brillouin zone sampling used 8x8x8 Monkhorst-Pack grids. Computations were performed on an Intel Xeon Gold 5218 CPU at Presidency University, Kolkata.

4. The objective of this thesis and the main accomplishments made in that regard

4.1. Characterization of polycrystalline bulk ferroelectric $ZnSnS_3$ synthesized by hydrothermal method for photovoltaic application

Synthesis- For the synthesis of $ZnSnS_3$ material, zinc nitrate hexahydrate [$Zn(NO_3)_2.6H_2O$], Tin(II) chloride [$SnCl_2$], and thiourea [CH_4N_2S] were used. A solution of 30 ml deionized water containing 1 mole of $Zn(NO_3)_2.6H_2O$, 1 mole of $SnCl_2$, and 3.6 moles of CH_4N_2S, with a few

drops of HCl, was stirred for 1 hour at room temperature and then sonicated for 2 hours. The mixture was transferred to a Teflon-lined autoclave and heated at 180°C for 16 hours. The resulting material was washed several times with deionized water to remove excess chemicals and dried at 110°C for 6 hours.

Results and Discussion

Microstructural study: The XRD pattern (Fig. 4.1.1a) shows numerous prominent peaks (indicated in fig.) that align well with the theoretically calculated XRD profile (Fig. 4.1.1b) for $ZnSnS_3$, obtained using VESTA software. These peaks correspond to various crystal planes of the trigonal $ZnSnS_3$ (space group-R3c, number-161) structure. The inter-planar spacing values range from 0.12 to 0.34 nm. A Williamson-Hall (W-H) plot (Fig. 4.1.1c) reveals a lattice strain of ~0.002 and an estimated grain size of ~15 nm. The lattice parameters are calculated as $a = b = c = 0.6773$ nm.

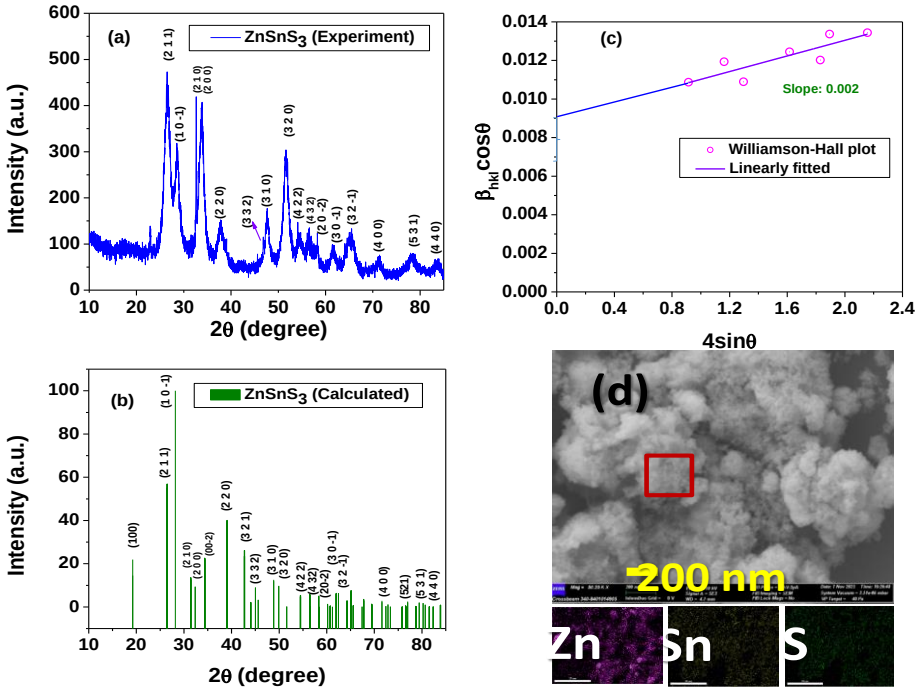

Figure 4.1.1 (a) XRD pattern of as grown $ZnSnS_3$ powder, **(b)** theoretically calculated XRD lines, **(c)** Williamson-Hall plot, and **(d)** FESEM image with elemental mapping.

Morphological study: FESEM image of the synthesized powder (Fig. 4.1.1d), showing nearly uniform spherical particles. The EDS spectrum confirms the presence of Zn, Sn, and S in

almost appropriate ratio near the surface, with elemental mapping indicating a uniform distribution of these elements.

The distribution of $ZnSnS_3$ nanoparticles was analysed using high-resolution transmission electron microscopy (HRTEM). The TEM micrograph (Fig. 4.1.2) revealed well-distributed particles, with grain size distribution mainly between 3 and 13 nm, and an average size of 7 nm. The HRTEM images showed clear lattice fringes, with interplanar spacing of 0.317 nm, 0.250 nm, and 0.228 nm, corresponding to the $(10\bar{1})$, (210), and (220) planes, respectively. These observations are supported by X-ray diffraction analysis (Table-4.1.1).

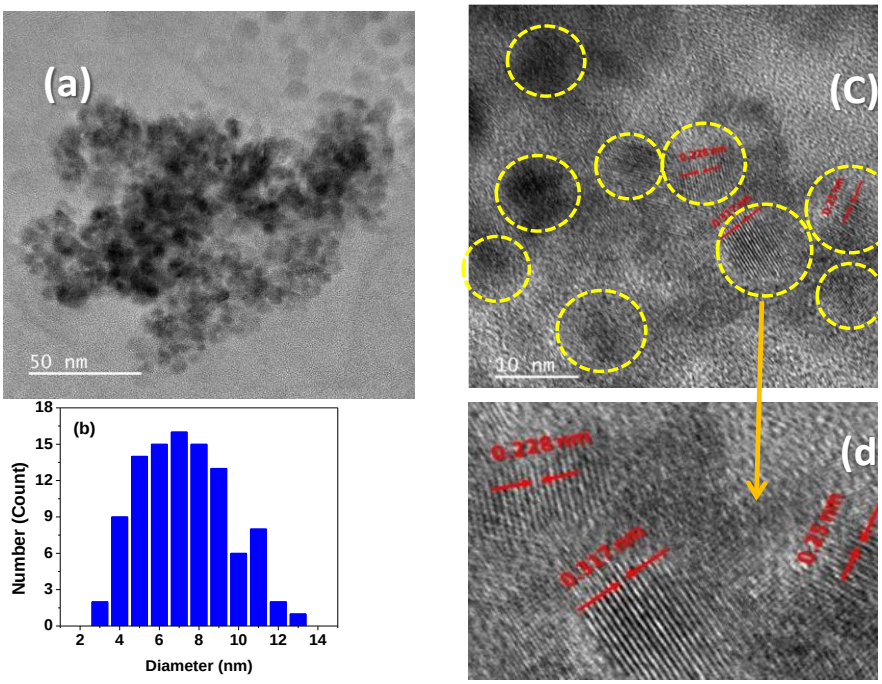

Figure4.1.2 (a) Bright field TEM image of $ZnSnS_3$, **(b)** grain size distribution of 100 particles from TEM, **(c)** crystal planes with labelled spacing, and **(d)** expanded view of the planes.

Table 4.1.1: Extracted parameters (interplanar distance (d), lattice planes (hkl), lattice constant and particle size) of $ZnSnS_3$ powder from XRD and TEM analysis.

2θ value (XRD)	'd' (nm) XRD	'd' (nm) TEM	(hkl) planes	'd' (nm) ASTM data	Lattice constant 'a' (nm)	Particle size (nm)
26.57	0.336	-	2 1 1	0.341	0.674	6.53
28.52	0.312	0.317	$1\ 0\ \bar{1}$	0.322	0.667	7.74

33.80	0.265	0.250	2 1 0	0.265	0.649	7.98
37.87	0.237	0.228	2 2 0	0.234	0.695	5.83
47.68	0.191	-	3 1 0	0.189	0.692	10.34
51.63	0.177	-	3 2 0	0.180	0.676	8.49
65.40	0.143	-	3 2 $\bar{1}$	0.144	0.675	5.07
71.30	0.132	-	4 0 0	0.133	0.687	7.94

Optical properties: Diffuse reflectance and absorbance of as-grown $ZnSnS_3$ powder were measured in the 300-800 nm wavelength range at room temperature. Fig. 4.1.3(a) illustrates transmittance, absorption, and reflectance, indicating good absorption in the visible spectrum, suggesting $ZnSnS_3$'s potential for solar cells and photovoltaics. The optical bandgap was analyzed using a Tauc plot and Kubelka-Munk function (F), derived from the reflectance data (R) by the relation [11, 24],

$$F = \frac{(1-R)^2}{2R} \tag{4.1.1}$$

Optical bandgap is measured (Fig. 4.1.3(b-d)) from the Tauc plot i.e. $(Fh\nu)^n$ vs $(h\nu)$ plot [NB: n=2 and 0.5 for direct and indirect transition respectively]. These analysis reveals direct band gaps at 2.62 eV and 3.13 eV, along with an indirect bandgap of 1.55 eV (Fig. 4.1.3c).

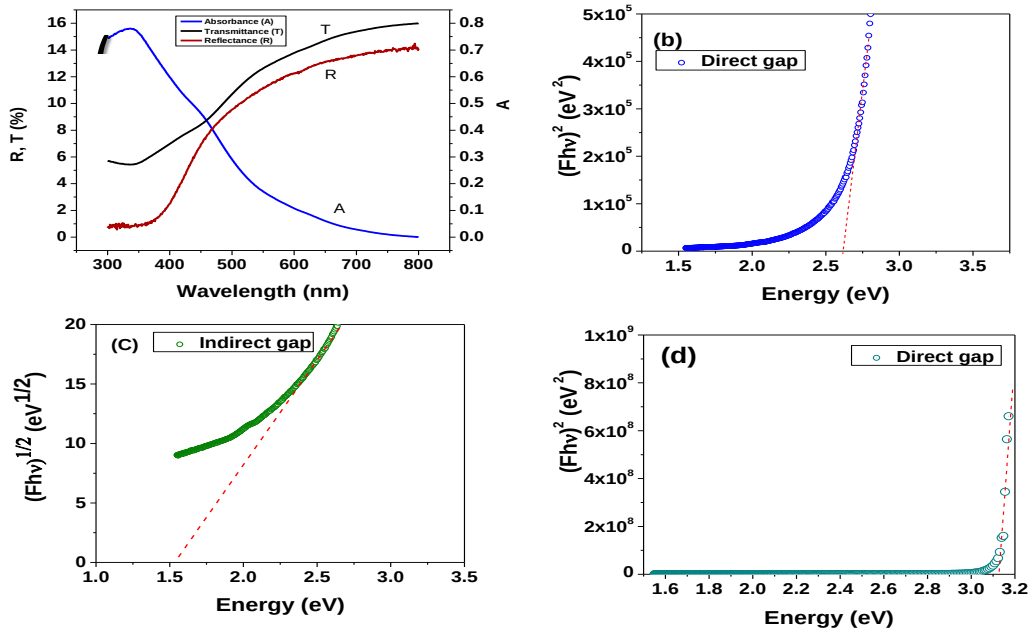

Fig. 4.1.3 (a) Absorbance (A), transmittance (T) and diffused reflectance (R) spectra of as prepared $ZnSnS_3$ obtained from UV-Vis-NIR spectroscopy, **(b, d)** $(Fh\nu)^2$ vs hν plot for estimating direct bandgap, and **(c)** $(Fh\nu)^{1/2}$ vs hν plot for estimating indirect bandgap using Kubelka-Munk function (F).

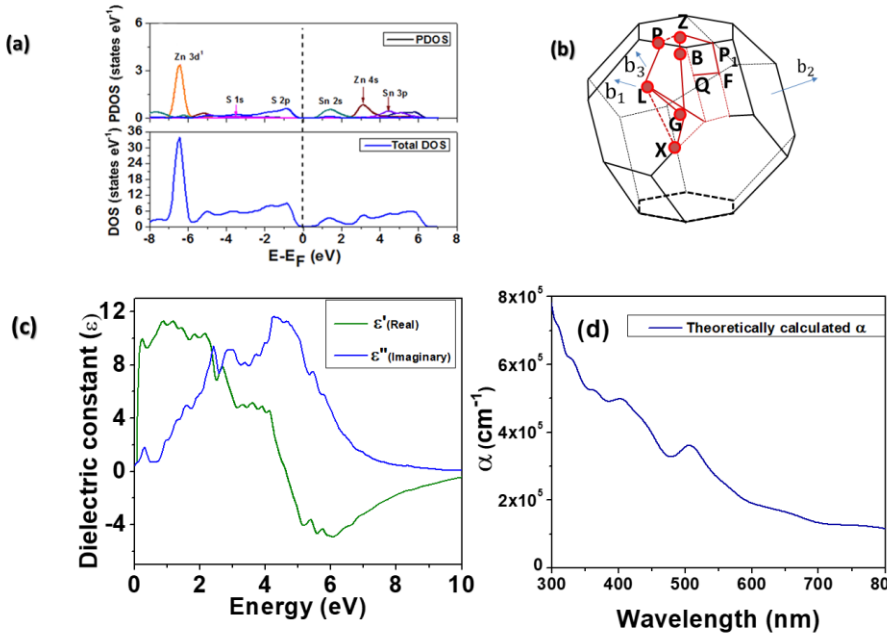

Fig. 4.1.4 (a) Density of states, **(b)** the first Brillouin Zone with high symmetry points **(c)** real and imaginary part (ϵ', ϵ'') of the dielectric function, and **(d)** the absorption spectra (α) of $ZnSnS_3$.

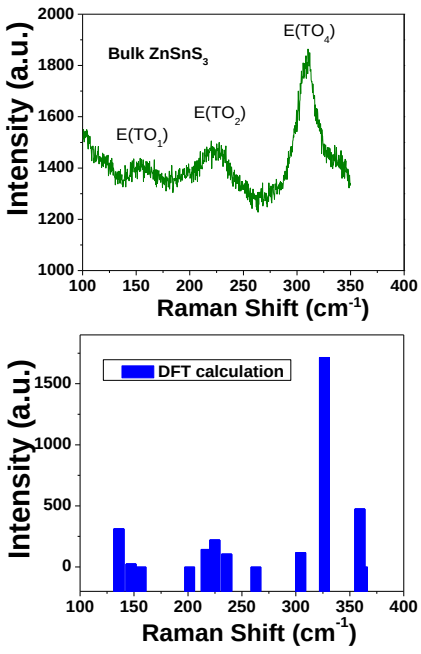

Figure 4.1.5 Obtained Raman spectrum of (a) as grown $ZnSnS_3$ and (b) DFT based calculation of $ZnSnS_3$.

Theoretical band structure calculations (Fig. 2.1, using Quantum Espresso software) support these experimental findings, showing possible transitions (Fig. 2.1). Additionally, an indirect transition at 0.64 eV (G point) and two direct transitions at 2.10 eV (Z point) and 2.95 eV (near G point) are identified. The real and imaginary parts of the dielectric functions (Fig. 4.1.4(c-d)) were determined using finer grids, leading to the calculation of the absorption coefficient, $\alpha(\omega)$,

$$\alpha(\omega) = \frac{2\omega}{c}\left(\frac{\sqrt{\epsilon'^2+\epsilon''^2}-\epsilon'}{2}\right)^{1/2} \qquad (4.1.2)$$

Here ϵ' and ϵ'' corresponds to real and imaginary part of dielectric function. In $ZnSnS_3$, the lowest band gap energy is likely linked to the optical transition between the hybridized S2p states in the valence band (VB) and the Sn2s states in the conduction band (CB).

The Raman spectrum of the powder was recorded in the wave number range of 100 to 350 cm^{-1} using excitation wavelength 632 nm (Fig. 4.1.5a). Given

that ZnSnS3 has a trigonal perovskite structure with space group R3c and point group symmetry 3m, the unit cell contains 10 atoms, resulting in 27 optical modes. According to group theory, crystals with this symmetry are expected to have 22 Raman active modes (4A1 + 18E) and five silent modes (5A2) [25-27]. The experimental Raman spectrum reveals a few number of active phonon modes. These active Raman modes were identified by comparison with the DFT (perturbation) based calculation (Fig. 4.1.5b) by Quantum Espresso software.

Ferroelectric property study: A study on ferroelectric polarization (P) versus applied electric field (E) was conducted, using a Sawyer-Tower circuit (Fig. 4.1.6a) and a 50 Hz AC source. Room temperature P-E hysteresis loops (Fig. 4.1.6b) were obtained at voltages between 400 and 700 V, confirming the sample's ferroelectricity. The loop area increased with higher voltage, indicating spontaneous ferroelectricity. At 700 V, the $ZnSnS_3$ pellet exhibited a saturation polarization (P_s) of 21.85 μC/cm², remnant polarization (P_r) of 14.34 μC/cm², and coercive field (E_c) of 6.23 kV/cm.

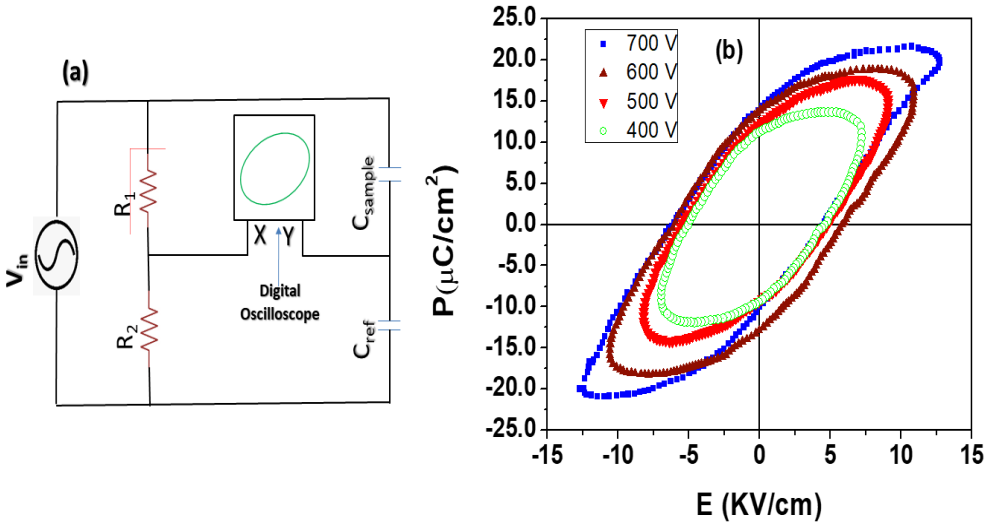

Figure 4.1.6 (a) Experimental set up for ferroelectric (P-E) observation and **(b)** P-E hysteresis loop at different input voltage

Phase transition: The Differential scanning calorimetry of grown $ZnSnS_3$ was performed and the DSC and TG curves (Fig. 4.1.7a) exhibit three exothermic peaks at 117°C, 332°C, and 460°C. The weight loss starting at 110°C corresponds to water evaporation, with the second peak linked to the tetragonal-to-monoclinic phase transition. The broad exothermic peak at 460°C suggests $ZnSnS_3$ dissociation into ZnS and SnS_2. Fig. 4.1.7(b) displays the dielectric constant's temperature dependence, showing peaks at 325°C and 480°C, likely indicating the phase transition and dissociation, aligning with the DSC data.

We have also theoretically calculated specific heat in the 30–800°C range using Lattice Dynamics (LADY) toolkits. Fig. 4.1.7(c-d) illustrate a crossover in specific heat curves near 330°C, indicating a phase transition from ferroelectric tetragonal to non-ferroelectric monoclinic $ZnSnS_3$.

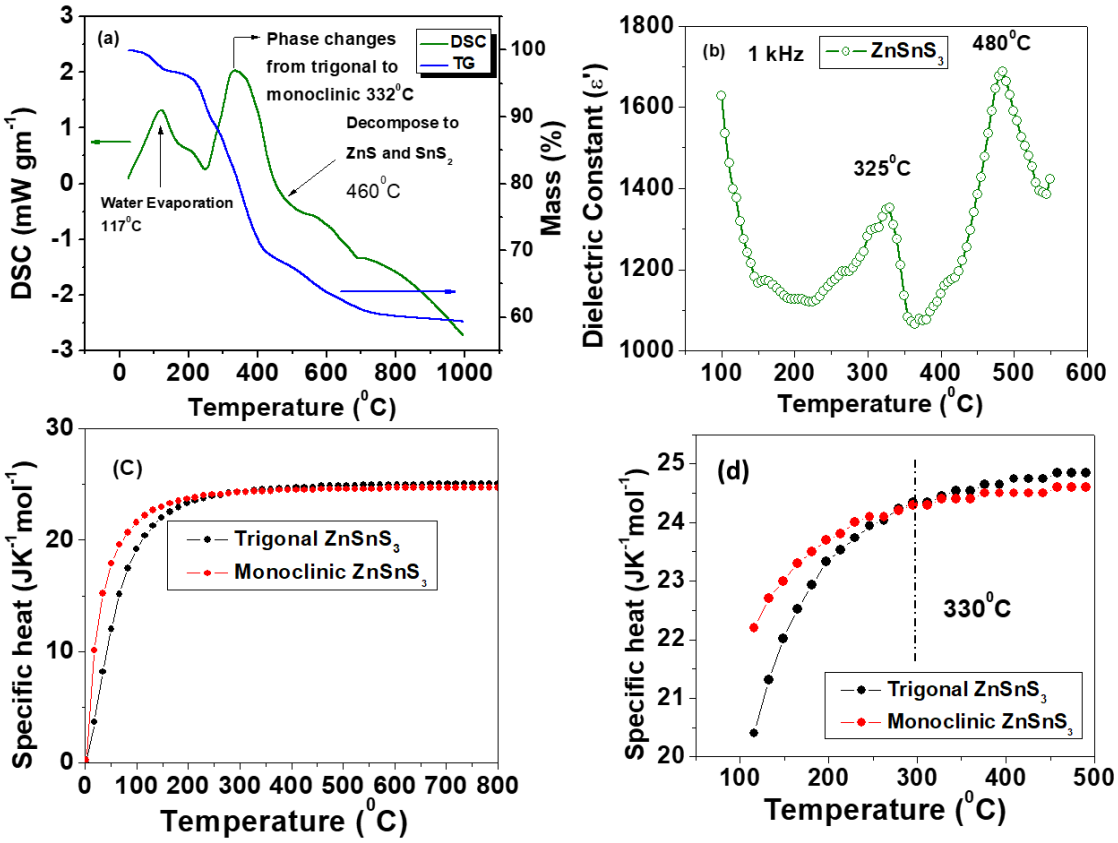

Figure 4.1.7 (a) DSC and TG curves of as grown $ZnSnS_3$, **(b)** real dielectric constant (ϵ') vs. temperature, and **(c-d)** temperature-dependent specific heat.

Photoluminescence study: Temperature-dependent photoluminescence (PL) measurements were performed to investigate point defects and optical recombination in $ZnSnS_3$. The spectra recorded from 4 to 300 K, shown in Fig. 4.1.8, exhibit asymmetrical profiles with two broad overlapping peaks. De-convolution of these spectra, exemplified by Fig. 4.1.8(b) for 300 K. At 4K the peaks at approximately 391 nm (3.11 eV) and 454 nm (2.73 eV) shift to lower energies and decrease in intensity with increasing temperature. The temperature dependence of these peak energies (Fig. 4.1.9a) was analysed using the empirical Varshni model,

$$E_{max}(T) = E(0) - \frac{\alpha T^2}{\beta + T}, \qquad (4.1.3)$$

Here E (0) represent PL emission peak at 0 K, and α and β are fitting parameters related to thermal expansion coefficient and Debye temperature of the material. The parameter values for the high and low energy peaks are E(0) = 3.11 eV, $\alpha = 3.92\times10^{-4}$ eV/K, β = 166 K, and E(0) = 2.73 eV, $\alpha = 6.51\times10^{-4}$ eV/K, β = 192 K, respectively. These peaks correspond to transitions from nearby donor levels to the valence band, as observed in the reflectance spectra (Figs. 4.1.3(b, d)). The broad PL peaks across temperatures likely result from radiative transitions from distributed donor levels to valence bands and the presence of nanoscale crystallites, which affect quantum size effects [28]. However, an indirect band gap of ~1.55 eV is seen in optical absorption spectra, this transition is not evident in the PL spectra even at 4K. $ZnSnS_3$ exhibit n-type conductivity as seen by hot-probe method. The most likely donors are Sn-on-Zn sites

[Sn_{Zn}] or S vacancy [V_S] though nothing is available for comparison. For two group of emission peak donor energies are estimated as $\varepsilon_D^1 = 23\text{meV}$, $\varepsilon_D^2 = 103\text{meV}$ at 300K using Eagle's equation [29],

$$\varepsilon_D^{1,2} = E_g^{1,2}(T) - h\nu_{PL}^{1,2} + \frac{1}{2}k_B T \tag{4.1.4}$$

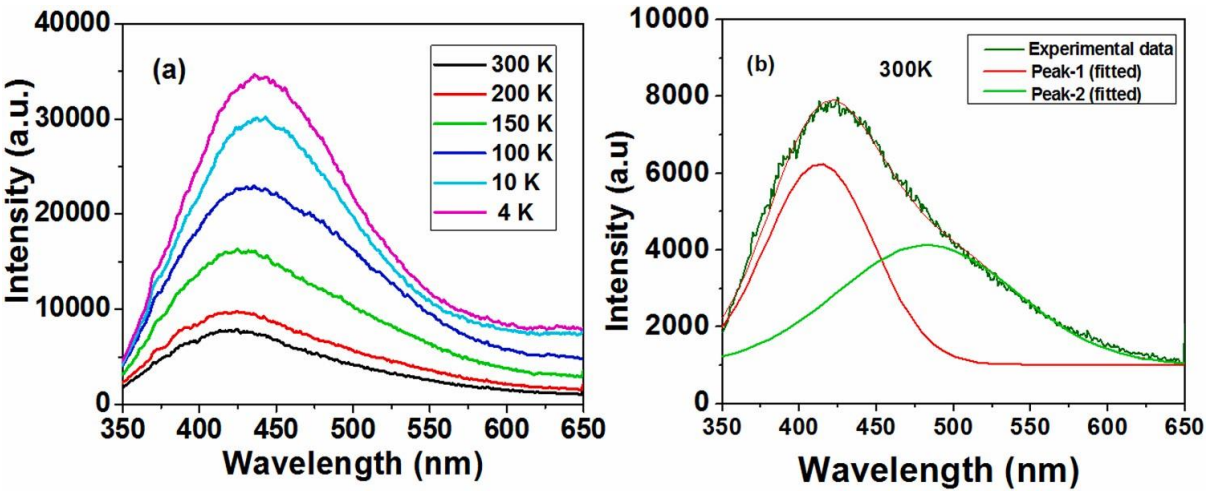

Figure 4.1.8 (a) PL spectra of $ZnSnS_3$ as function of temperature and **(b)** de-convoluted PL spectra recorded at 300K.

Intensities (integrated) of both PL peaks with inverse temperature is shown (Fig. 4.1.9b) and fitted with two channel Arrhenius equation [30],

$$I = \frac{I_0}{1+A\exp\left(\frac{-E_{T1}}{KT}\right)+B\exp\left(\frac{-E_{T2}}{KT}\right)} \tag{4.1.5}$$

A and B are constant where E_{T1} and E_{T2} linked to two activation energies at low and high temperature regions. For peak-2, E_{T1}=46 meV and E_{T2}=0.64 meV; for peak-1, E_{T1}=0.09 meV and E_{T2}=30 meV, indicating two thermally activated recombination centers. The diffuse reflectance measurements indicate two direct optical transitions at 2.62 eV and 3.13 eV at room temperature, so the PL emission bands around 2.61 eV and 3.04 eV are unlikely to result from band-to-band transitions in $ZnSnS_3$. The activation energies are linked to the thermal quenching of photoluminescence intensity, primarily due to nonradiative decay channels of photo-excited carriers. At very low temperatures (4K in our study), most excited carriers are confined near the bottom of the conduction band with a narrow energy distribution, leading to strong emission intensity. As temperature increases, carrier decay through non-radiative channels becomes significant. The energy level of these non-radiative channels is typically defined by activation energy. A lower activation energy leads to quicker thermal quenching of PL intensity. In our sample, two activation energies were detected at 0.09 meV and 30 meV for peak-1. Based on these study a model for possible transition is shown in Fig. 4.1.10.

We analysed the variation in peak energy and integrated intensity of two PL emission bands with excitation power at 4K, as shown in Fig. 4.1.11. Figs. 4.1.12 illustrate how PL intensity changes with laser power (16.8-100 mW). The similar quenching behavior of the two emission

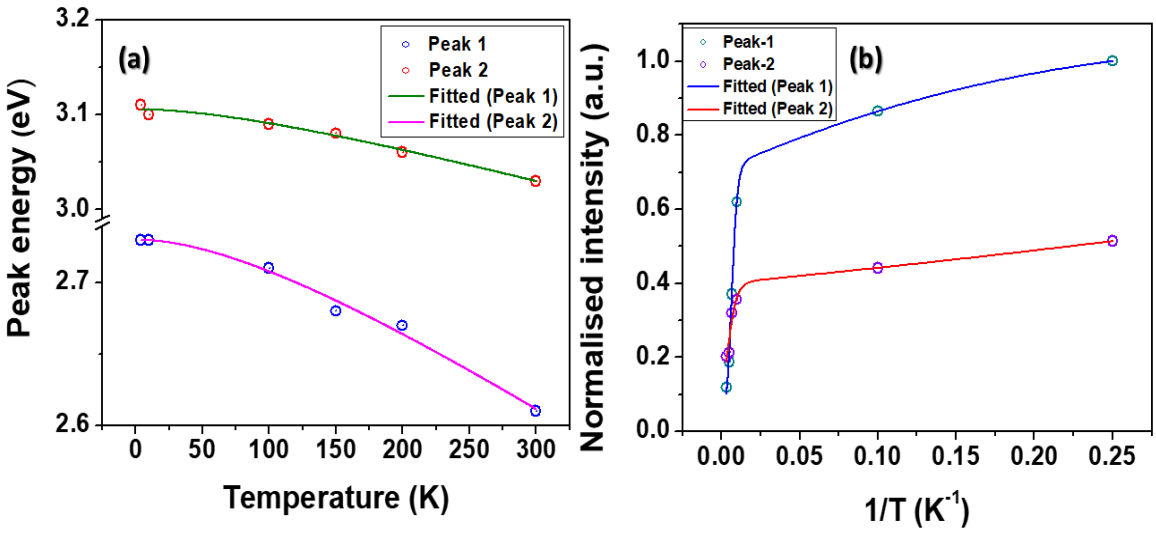

Figure 4.1.9 (a) Peak energy of both group of de-convoluted peaks as function of temperature and **(b)** intensities (normalised) as function of inverse temperature.

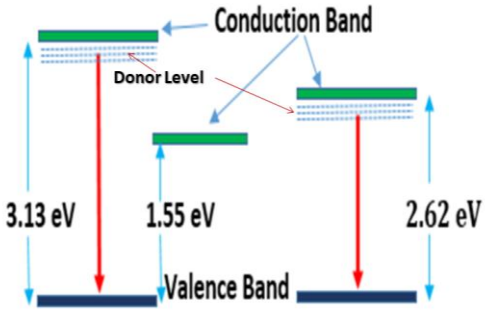

Figure 4.1.10 Schematics of possible optical transition (dotted line indicate the donor level).

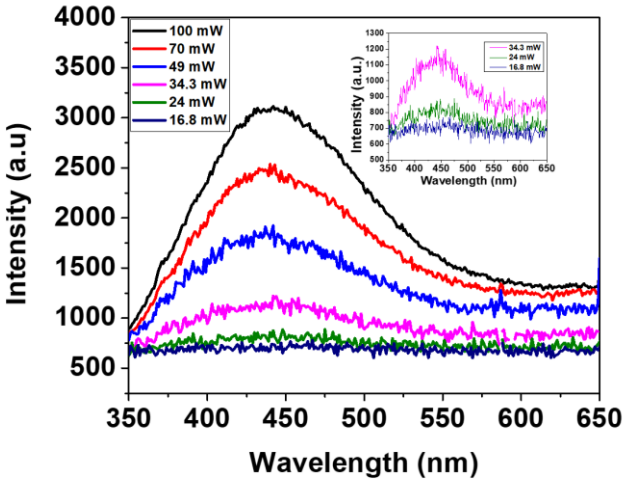

Figure 4.1.11 PL spectra of $ZnSnS_3$ with different laser excitation power obtained at 4K and spectra with lowest three excitation power (inset).

peaks suggests a common origin. Additionally, as the PL peak energies red-shifted, the emission intensities increased exponentially with excitation power for both peaks. These findings suggest the presence of shallow and deep-level defect-related PL transitions in the sample [29]. Based on the optical band gap measurements and PL peak energies at different temperatures, the as-grown $ZnSnS_3$ sample likely shows recombination processes from donor (D) levels to the valence band. The PL emission intensity follows a power law relationship, $I_{PL} \propto P^n$, with excitation power (P). The fitted parameters (n = 1.23 and 1.67) for the two emission groups align well with a model from the literature [31]. According to the model, the reduction in PL peak energy with increased excitation power is due to higher donor energy of the charge carriers, indicating that deeper donor levels are ionized at higher laser powers.

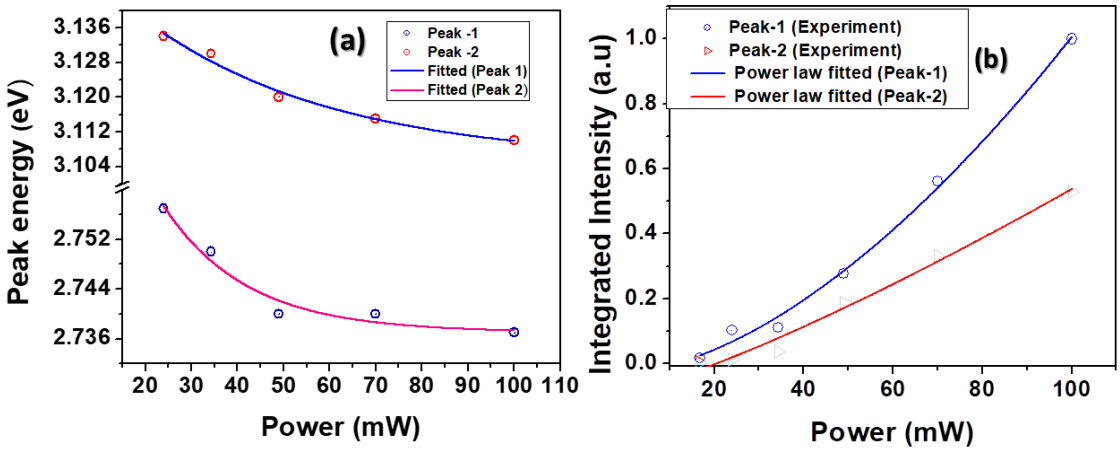

Figure 4.1.12 (a) Normalised peak intensity of both peaks as function of excitation power and **(b)** variation of peak energy of those peaks with excitation power

Current-Voltage characteristics: The current-voltage (I-V) characteristics of the Ni/$ZnSnS_3$/Ni device were examined in dark conditions and under 532 nm and 650 nm illumination (5.0 mW). The sample was illuminated on its cylindrical surface (inset, Fig. 4.1.13(a)). To study polarization switching, the device was poled upward and downward by applying a 25V DC bias for 60 minutes. Fig. 4.1.13(a) shows the I-V characteristics of the virgin sample under both conditions. Illumination clearly affects the I-V response, indicating the photovoltaic behavior of $ZnSnS_3$. No dark current was observed at zero bias, but a positive photocurrent and an open-circuit voltage suggest the presence of an internal field, likely due to polarization. Fig. 4.1.13 (b) displays the I-V characteristics of the device in darkness and under light after downward and upward poling. Table-4.1.2 lists the saturation currents (I_{SC}) and open circuit voltages (V_{OC}) for different conditions, confirming a polarization-induced photovoltaic response in the Ni/$ZnSnS_3$/Ni device. The details analysis is done in the next section.

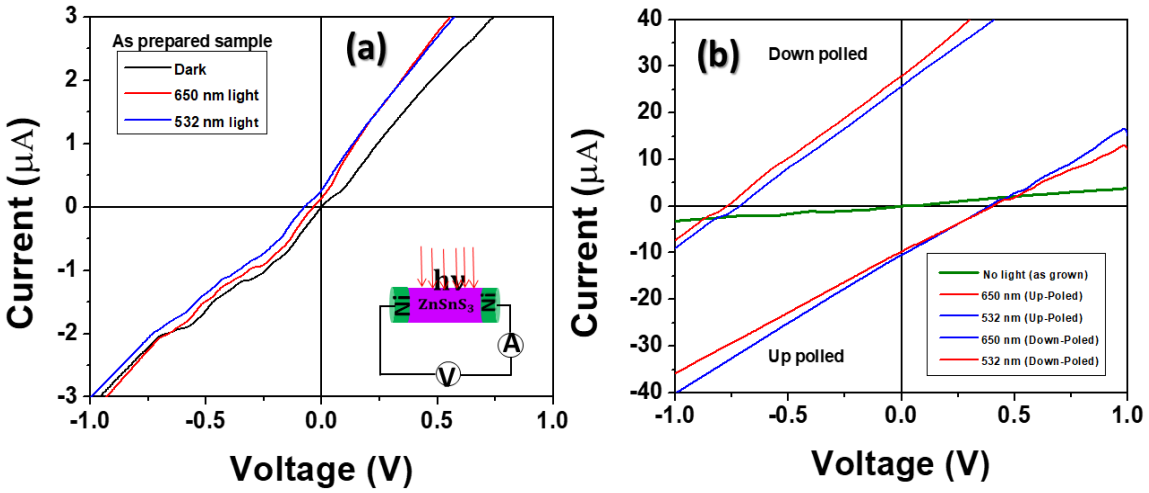

Figure 4.1.13 Current-voltage characteristics of Ni/$ZnSnS_3$/Ni structure with different illumination for **(a)** as grown (device structure is shown in inset) and **(b)** up-poled and down-poled sample.

Table-4.1.2 Saturation current (I_{SC}) and open circuit voltage (V_{OC}) of the as grown and poled sample under different incident wavelength.

Illumination	As-grown sample		Up-poled sample		Down-poled sample	
wavelength	I_{sc} (μA)	V_{oc} (V)	I_{sc} (μA)	V_{oc} (V)	I_{sc} (μA)	V_{oc} (V)
650 nm	0.125	-0.034	-10.68	0.410	27.87	-0.768
532 nm	0.246	-0.071	-10.03	0.396	25.60	-0.710

4.2. Ferroelectric $ZnSnS_3$ thin films: growth and measurement of photovoltaic properties

Synthesis- Thin films LN-$ZnSnS_3$, with a nominal thickness of 900–1000 nm, were deposited on quartz, sapphire, glass coated with fluorinated tin oxide (FTO), and silicon (001) substrates. The films were produced using a spray pyrolysis technique, utilizing a precursor solution composed of 50 ml of a water-ethyl alcohol mixture (1:3 ratio), containing 0.01 mol of $ZnSn(OH)_6$ and 0.08 mol of thiourea (NH_2CSNH_2). The spray was performed at elevated temperatures (300–350 °C), other growth parameters were optimized, including pressure (~3 Bar), spray distance from the substrate (10–15 cm), and growth duration (5–10 minutes). For the preparation of $ZnSn(OH)_6$, 50 ml of 0.1 M $Na_2SnO_3{\cdot}H_2O$ solution in a water-ethylene glycol mixture (1:3) was gradually mixed into 50 ml of 0.1 M $Zn(CH_3COO)_2{\cdot}H_2O$ in the same water-ethylene glycol ratio (1:3) [24].

Results and Discussion

Structural and morphological characteristics: The GIXRD (grazing incidence x-ray diffraction) experiment was performed of the as grown sample and the recorded pattern (Fig. 4.2.1a) shows prominent diffraction peaks, which are indexed and closely match the calculated x-ray diffraction pattern (Fig. 4.2.1b) generated with VESTA software and indexed to $ZnSnS_3$ (JCPDS 28-1486). The average particle size, determined using the Scherrer equation, is approximately 8–10 nm. The lattice parameters are calculated and obtained as a = b = c = 0.6766 nm.

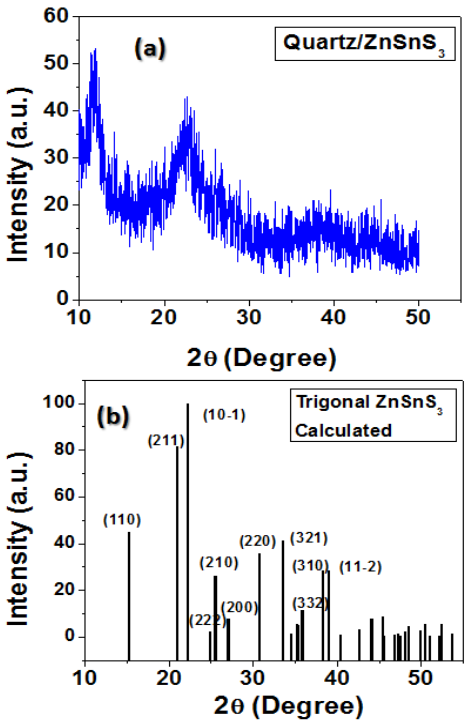

Figure 4.2.1 a) GIXRD pattern of as grown $ZnSnS_3$ and **b)** software generated XRD spectrum of trigonal (R3c) $ZnSnS_3$.

The morphological study observed by FESEM is presented in Fig. 4.2.2a, which reveals that the synthesized $ZnSnS_3$ thin films exhibit uniformly distributed spherical particles. The EDS spectra shown in Fig. 4.2.2b confirm the presence of Zn, Sn, and S elements, which are homogeneously distributed across the film surface, as depicted in the elemental mapping images in Fig. 4.2.2(c–e).

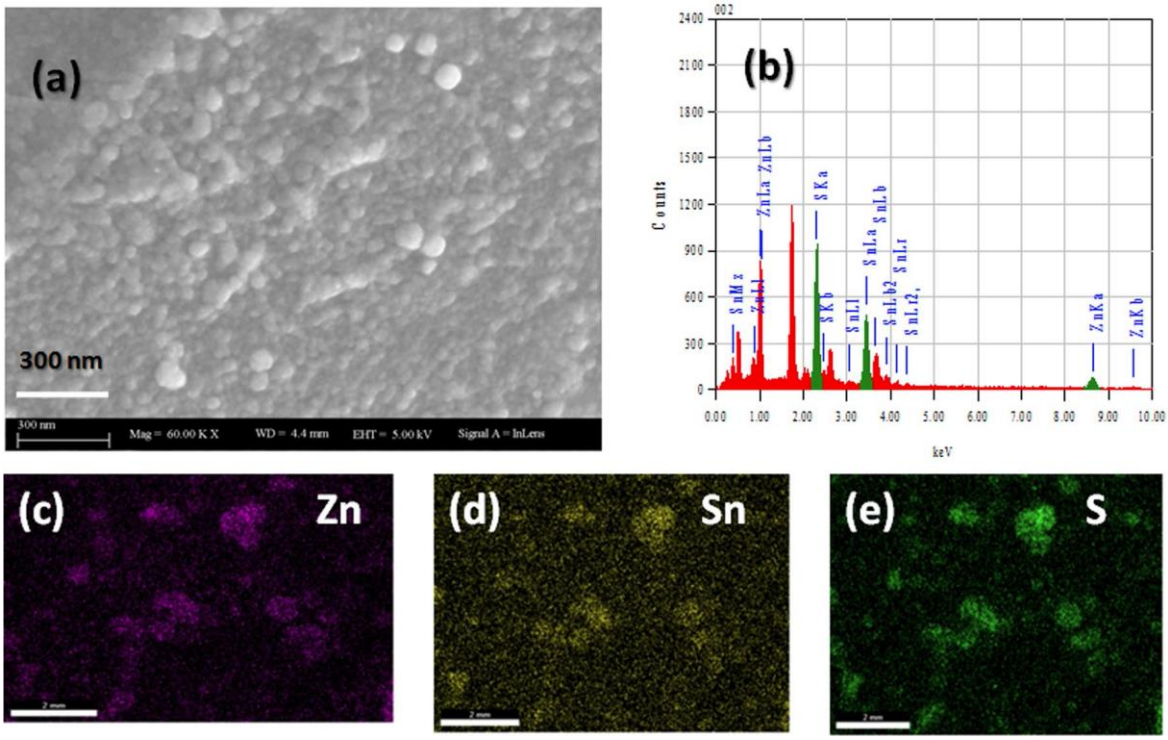

Figure 4.2.2 a) FESEM micrograph, **b)** EDS spectrum and **c**–**e)** elemental mapping of Zn, Sn and S in $ZnSnS_3$ thin films on silicon substrate.

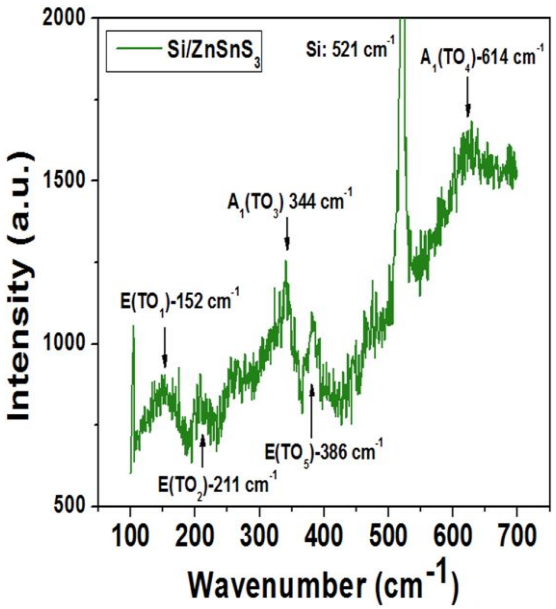

Figure 4.2.3 Raman spectrum of $ZnSnS_3$ thin film deposited on silicon substrate.

Raman study: The Raman spectrum of the $ZnSnS_3$ film was recorded in the wave number range of 100 to 700 cm^{-1}. The experimental Raman spectrum of the ZnSnS3 film reveals a few Raman active phonon modes (A1-TO, E-TO) at wavenumbers 152, 211, 262, 344, 386, and 614 cm^{-1} (Fig. 4.2.3a). These active Raman active modes were identified by comparison with the reported Raman spectrum of $LiNbO_3$ crystal, which shares similar space group symmetry [25-27].

Bandgap and absorbance study: Figure 4.2.4a presents the diffuse reflectance (R), transmittance (T), and absorbance (A) of the $ZnSnS_3$ thin film of approximately 900 nm thick, deposited on quartz substrates at 300°C. The optical properties of the $ZnSnS_3$ thin film demonstrate strong absorption with

minimal reflectance in the visible range, highlighting its potential for solar cell applications. The absorption coefficient (α) of the films is determined using the given relation

$$\alpha = \frac{1}{t} ln \frac{(1-R)^2}{T} \quad (4.2.1)$$

The absorption coefficient (α) is found to be in the range of 6.5×10^4 cm^{-1}–7.0×10^4 cm^{-1} for the visible range of the solar spectrum and shown in Fig. 4.2.4b. The type and magnitude of optical bandgap is studied in same way using Tauc plot (shown in Fig. 4.2.4c) as stated in previous section. We have identified a direct band gap transition at 2.62 eV and an indirect optical transition at 1.63 eV (shown in inset of Fig. 4.2.4c). (shown in Fig. 4.2.4c) as stated in previous section. We have identified a direct band gap transition at 2.62 eV and an indirect optical transition at 1.63 eV (shown in inset of Fig. 4.2.4c). The observed direct band gap of 2.62 eV is significantly higher than the theoretically predicted value (~1.30 eV) from DFT calculations [19, 20].

However, the indirect band gap of 1.63 eV is more closely aligned with the theoretical predictions. It is important to note that the nature and magnitude of the band gap can vary significantly depending on the approximation used in first-principles calculations [32]. Additionally, the band gap widening could be attributed to the smaller crystallite size of the $ZnSnS_3$ films, indicating a quantum size effect.

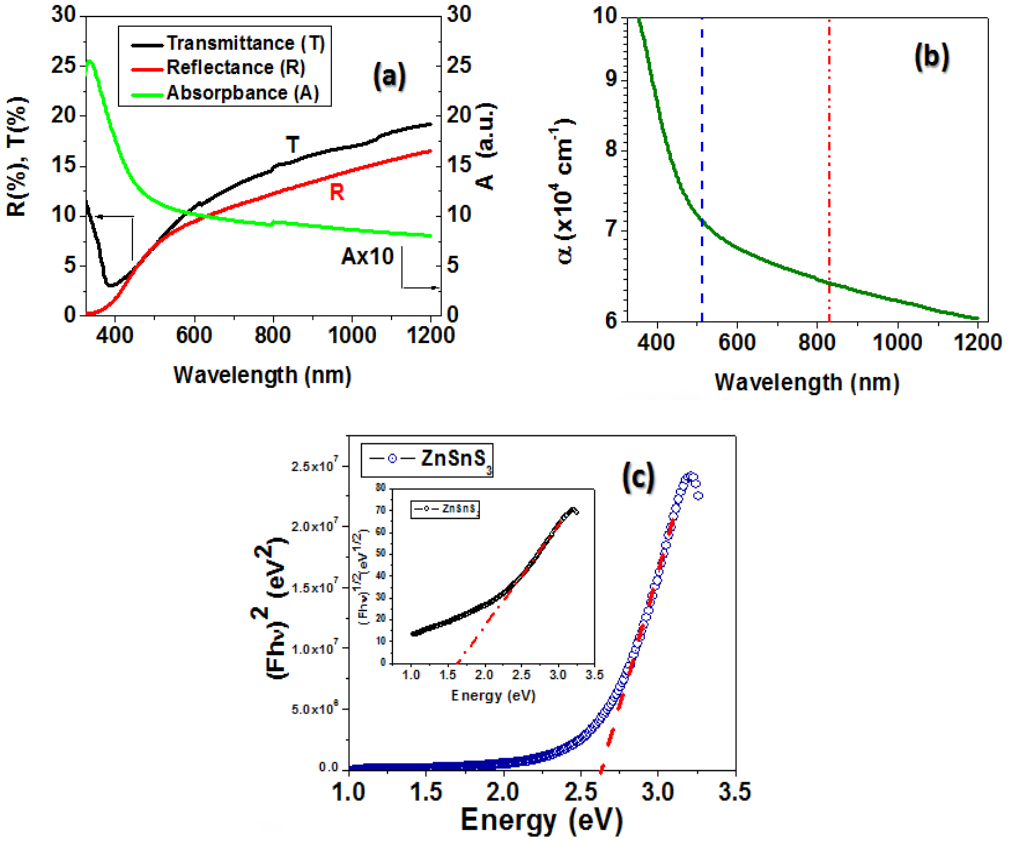

Figure 4.2.4 (a) Diffused reflectance (R), transmittance (T), and absorbance (A) spectra of $ZnSnS_3$ on quartz substrate, **(b)** absorption coefficient (α) as function of wavelength, and **(c)** $(Fh\nu)^2$ vs $h\nu$ plot using Kubelka-Munk function (F) for calculating optical bandgap.

Ferroelectric property study: For the ferroelectric study the device Ni/$ZnSnS_3$/FTO is made (Fig. 4.2.5b) and the room temperature P–E hysteresis loop (Fig. 4.2.5a) was measured at 100 Hz using a Sawyer‑Tower circuit. The result reveal clear evidence of ferroelectricity in the films and the observed hysteresis is linked to ferroelectric polarization, with a saturated polarization of 20.5 μC/cm², which is also found light-sensitive (Fig. 4.2.5c). The remnant polarization is 12.10 μC/cm², and the coercive field is measured at 16 kV/cm.

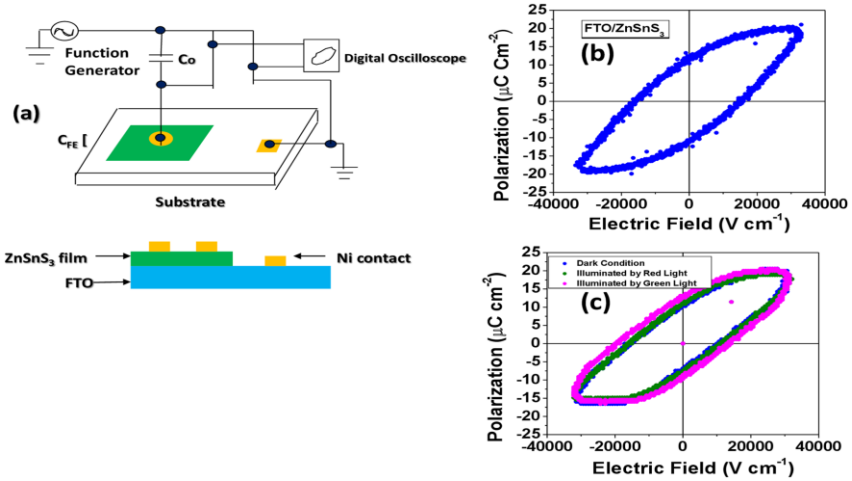

Fig 4.2.5 (a) The experimental setup and substrate–film configuration for ferroelectric study, **(b)** obtained polarization (P) versus electric field (E) loop, and **(c)** P–E loops under light illumination (λ = 532 nm) of Ni/$ZnSnS_3$/FTO structure.

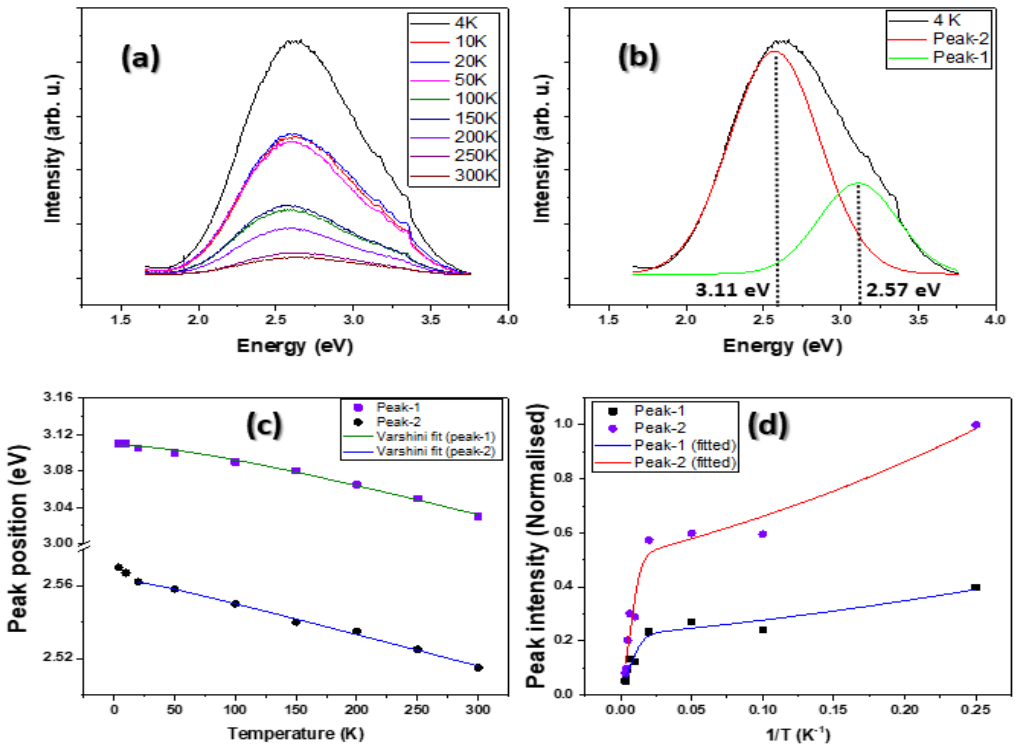

Figure 4.2.6 (a) Temperature varying PL spectra of $ZnSnS_3$ thin film deposited on Si (001), **(b)** de-convoluted PL peak obtained at 4K, **(c)** peak energy position of Peak-1 and Peak-2 with fitted by Varshini equation as function of temperature, and **(d)** both peak's normalised intensity variation with fitted by Arrhenius equation with reciprocal temperature.

Photoluminescence study: A typical photoluminescence (PL) spectrum of $ZnSnS_3$ thin film are carried out in the same way as it is done for powder (discussed in previous section). The findings about possible transition and quenching nature are almost similar with bulk $ZnSnS_3$, so only the images like PL spectra, peak energy and intensity with fittings are presented here (Fig. 4.2.6 and Fig. 4.2.7).

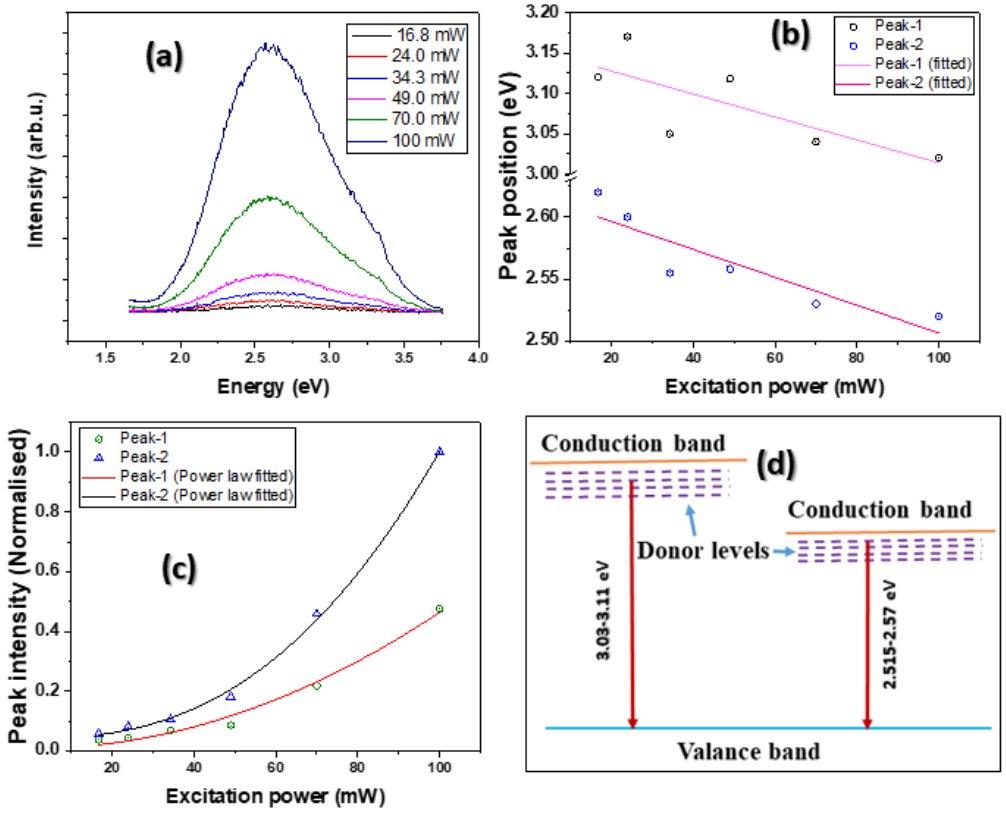

Figure 4.2.7 (a) Excitation laser power varying PL spectra at fixed temperature 4K, **(b)** peak energy position of two peaks with linear fitting as function of excitation power **(c)** dependence of intensities of the peaks (with power law fitting) on laser incident power, and **(d)** suggested model for possible optical transition.

Current-Voltage characteristics: The current–voltage (I–V) characteristics of the $Ni/ZnSnS_3/FTO$ device were measured at room temperature both in the dark and under laser illumination (5 mW, $\lambda = 532$ nm) using a Keithley 2450 source meter and the obtained results are shown in Fig 4.2.8a. Also, the device was poled with an external electric field of ±5 V. To achieve the downward (upward) polarization state, a +5 V (−5 V) external poling voltage was applied to the top Ni electrode of the $Ni/ZnSnS_3/FTO$ structure and I–V characteristic curves for P_{down} and P_{up} states, shown in Fig. 4.2.8b. To interpret the results, the energy band diagrams

under dark and illuminated conditions for both polarization directions, resulting from poling, are schematically illustrated in Fig. 4.2.9a–c.

We have used Ni's work function ($q\varphi_m$) as 5.15 eV and that of FTO as 5.0 eV, based on references [33, 34]. Since the electron affinity (χ) of $ZnSnS_3$ is not available in the literature, we estimated it by averaging the electron affinities of SnS_2 (4.16 eV) and ZnS (3.90 eV), resulting in a value of $q\chi$ = 4.03 eV [35, 36]. Although $ZnSnS_3$ films deposited by spray pyrolysis exhibit n-type conductivity (known from hot probe technique), the nature of the impurity levels remains unknown. We approximated the work function of $ZnSnS_3$ to be 4.68 eV, assuming the Fermi level is positioned one-fourth of the energy gap (E_g = 2.62 eV) from the conduction band minimum. Consequently, the barrier height ($q\phi_b'$) at the Ni/$ZnSnS_3$ interface is calculated as 1.12 eV for electrons, while that of the $ZnSnS_3$/FTO interface ($q\phi_b''$) is 0.97 eV, determined using the barrier height relation [37] for electron flow.

$$q\phi_{bi} = q\phi - q\chi \tag{4.2.3}$$

Since there is a difference in work function between electrodes and the film, certainly the built-in potential are not of similar nature. The differing work functions ($qV_{bi} = q\phi_{electrode} - q\phi_{ZnSnS_3}$), with values of $qV_{bi}' = 0.47$ eV and $qV_{bi}'' = 0.32$ eV, result in built-in electric fields with negative and positive slope respectively at $Ni - ZnSnS_3$ and $FTO - ZnSnS_3$ interface as shown in fig. 4.2.9b-c. This indicates that the built-in electric fields at these two interfaces are oriented in opposite directions. As a result, there is an indelible built-in potential ($qV_{bi}' - qV_{bi}''$) of -0.15 eV across the ferroelectric capacitor, directed from the FTO electrode towards the Ni electrode, as illustrated in fig. 4.2.9a which is also established by open circuit voltage (V_{OC}) of -0.12 V (Fig. 4.2.8a).

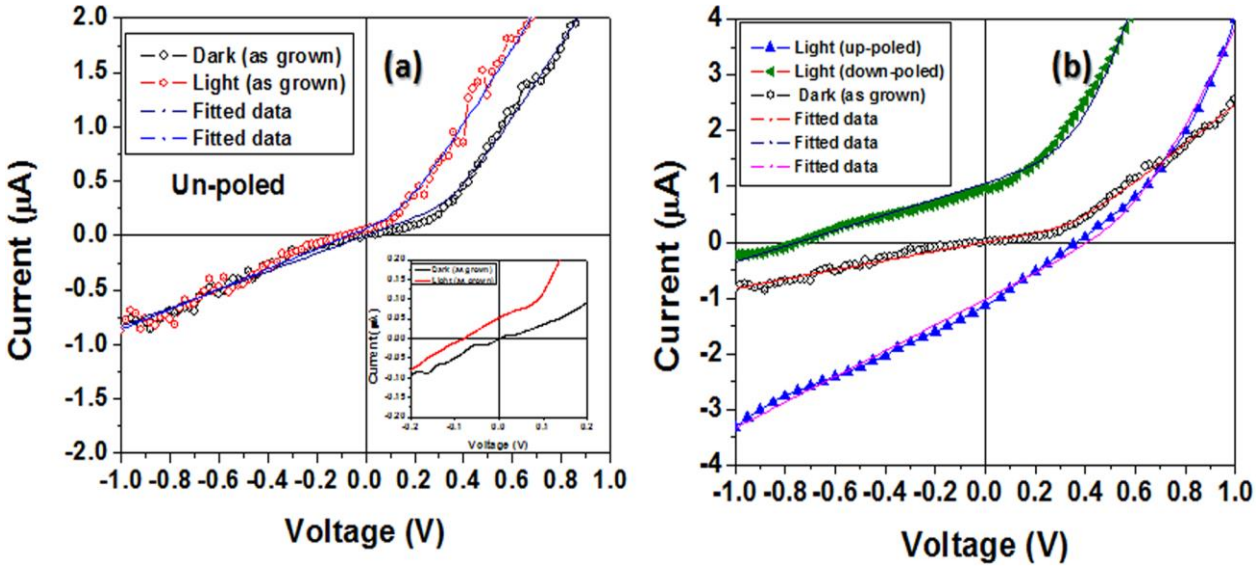

Figure 4.2.8 I–V characteristics of Ni/$ZnSnS_3$/FTO structure for **a)** unpoled and **b)** poled states. [*Illumination (λ = 532 nm) with power density (5.75 mW/cm^2)*]

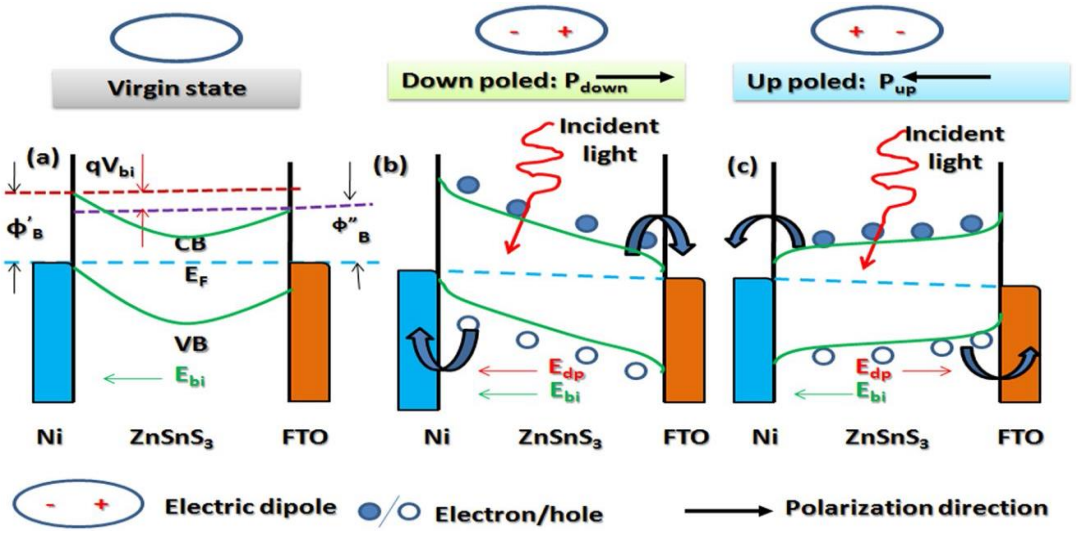

Figure 4.2.9 Schematic energy band structure of Ni/$ZnSnS_3$/FTO structure for **(a)** as grown (under no light), **(b)** down poled (with illumination), and **(c)** up poled (with illumination) conditions.

The calculated depolarization field is also calculated [38] and it is found $qV_{dp} = -0.61$ eV corresponds to a potential difference across the ferroelectric $ZnSnS_3$ capacitor between the Ni contact and the FTO substrate. For the downward polarization state (P_{down}), the Ni/$ZnSnS_3$ interface forms a nearly blocking (Schottky) contact, while the $ZnSnS_3$/FTO interface forms a non-blocking (ohmic) contact. Conversely, for the upward polarization state (P_{up}), the Ni/$ZnSnS_3$ interface becomes non-blocking, and the $ZnSnS_3$/FTO interface becomes blocking. Thus, the I–V characteristics at both interfaces can be modulated by changing the polarization direction of the $ZnSnS_3$ ferroelectric layer through appropriate poling processes [39]. Now for positively poled (P_{down}-state) it is expected to have open circuit voltage V_{OC} ($V_{bi}+V_{dp}$) to be -0.76 V which is quite close to the experimental observed -0.82 V. Also, for the other poled state (P_{up}-state) experimental observed $V_{OC} = 0.37$ is close to expected (0.46 V) value.

The nonlinear I-V curve obtained in Fig. 4.2.8 can be attributed to single Schottky barrier solar diode. The equivalent circuit is given in Fig. 4.2.10 consisting Schottky diode (D), a bulk resistance (R_B) due to ferroelectric $ZnSnS_3$ layer, a current source (I_{ph}) under illumination, and a shunt resistance (R_{sh}). The current voltage equations are,

$$I' = I_S\left(\exp\frac{q(V-I'R_B)}{nK_BT} - 1\right) + \frac{V-I'R_B}{R_S} \tag{4.2.4}$$

$$I' = I + I_{Ph} \tag{4.2.5}$$

$$\text{And, } I_S = AA^*T^2\exp\left(-\frac{q\phi_B}{K_BT}\right) \tag{4.2.6}$$

Here, A is a constant and A^* is the Richardson constant which is given by,

$$A^* = \frac{4\pi m_e^* q K_B^2}{h^3}$$

These equations are used to fit experimental curves using Lambert W function,

$$I = \frac{V}{R_B} - I_{Ph} - \frac{(I_S R_B + V)R_S}{R_B + R_S} + \frac{nK_BT}{qR_B} W\left[\frac{qI_S R_B R_S}{nK_BT(R_B+R_S)} \exp\left\{\frac{q(I_S R_B + V)R_S}{nK_BT(R_B+R_S)}\right\}\right] \quad (4.2.7)$$

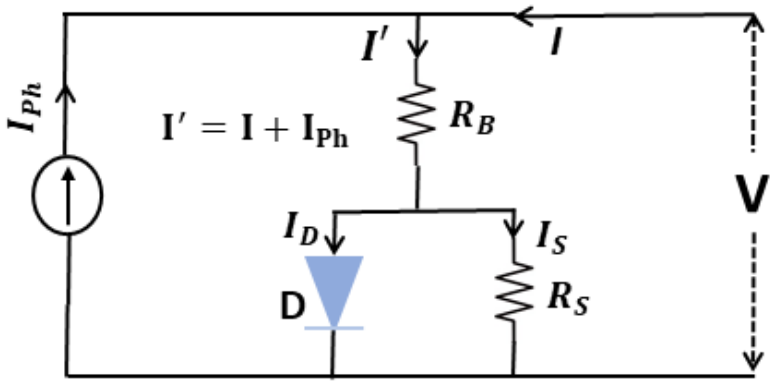

Figure 4.2.10 Schematic of current flow mechanism in $ZnSnS_3$ using Schottky model

Fitting the equations the parameters are obtained and represented in Table-4.2.1. If one ignore the Schottky effect, the I–V relationship can be described as,

$$I = V\frac{(\sigma+\sigma_{Ph})}{t}A - I_{Ph} \quad (4.2.8)$$

The power conversion efficiency for the downstate polarization of the device is found nearly 0.04% at 5.75 mW/cm^2 illumination power density.

Table-4.2.1 *The electrical parameters, obtained from the current-voltage (I-V) characteristics of Ni/$ZnSnS_3$/FTO devices under both dark conditions and when illuminated at a power density of 5.75 mW/cm² ($\lambda = 532\ nm$).*

Parameters	As-grown		Up-poled	Down-poled
	Dark	Illuminated	Illuminated	Illuminated
Barrier height, ϕ_B (eV)	0.93	0.77	0.79	0.74
Bulk resistance, R_B (KΩ)	279	273	85	53.3
Conductivity, σ (S/m)	0.81×10^{-6}	0.82×10^{-6}	2.65×10^{-6}	4.22×10^{-6}
Shunt resistance, R_S (KΩ)	924	809	346	661
Photocurrent, I_{Ph} (μA)	0	-0.06	1.06	-1.05
Open circuit voltage, V_{OC} (V)	0	-0.12	0.37	-0.82
Short circuit current, I_{SC} (μA)	0	0.06	-1.12	0.99

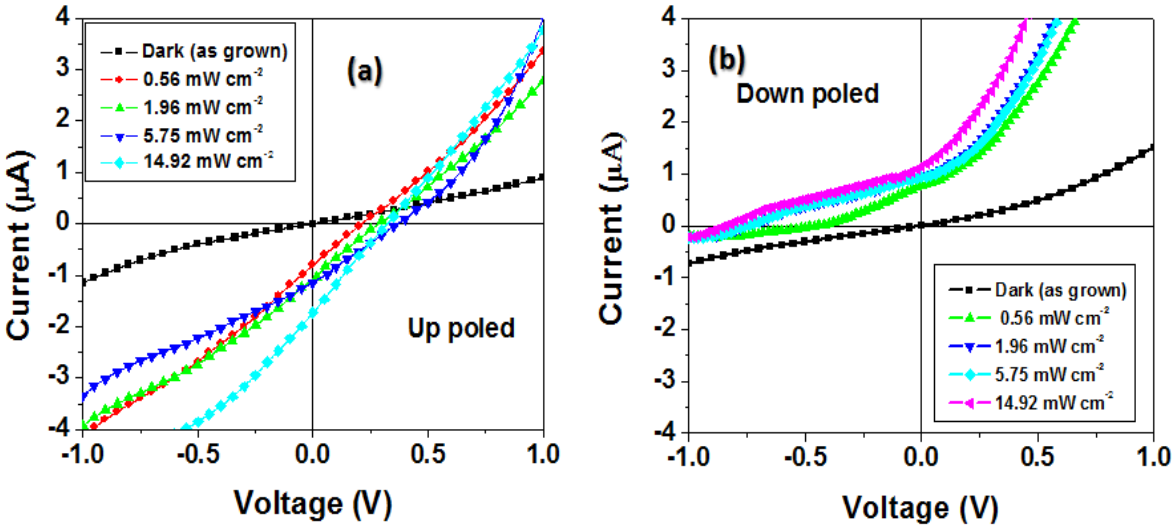

Figure 4.2.11 I-V characteristics under different incident laser power intensities of **(a)** up-poled, and **(b)** down-poled Ni/$ZnSnS_3$/FTO device at room temperature

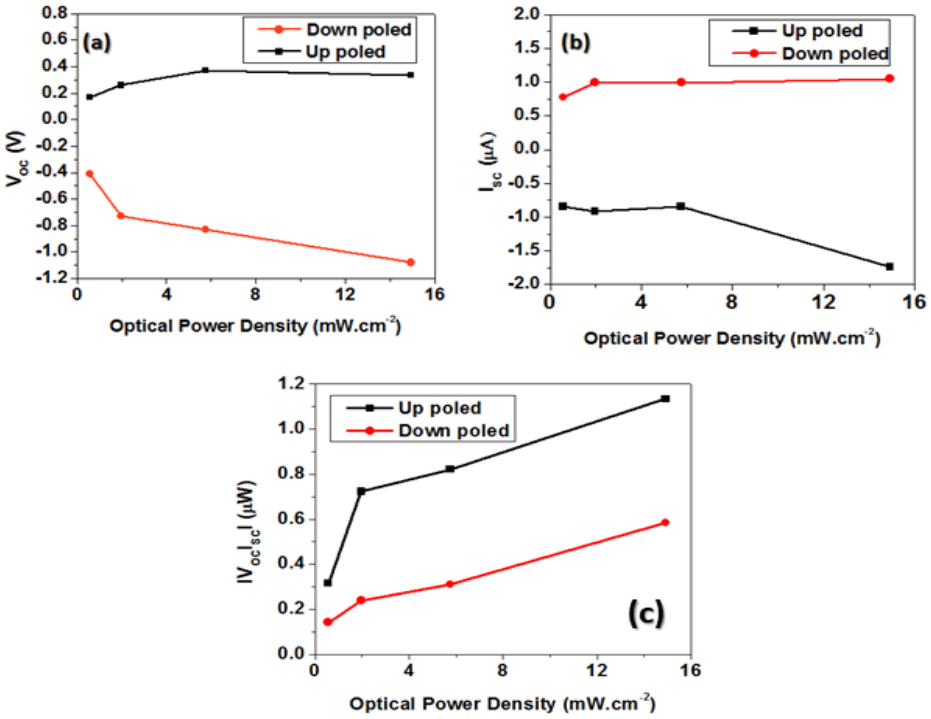

Figure 4.2.12 (a) open circuit voltage (V_{OC}), and **(b)** short circuit current (I_{SC}) variation of Ni/$ZnSnS_3$/FTO device with different optical power densities, and **(c)** Variations in the product of I_{SC} and V_{OC} with different optical power density.

The current–voltage (I-V) characteristics of Ni/$ZnSnS_3$/FTO devices under illumination (λ = 532 nm) were measured at various power densities (0.56–14.92 mW/cm²), as shown in Fig. 4.2.11. The effects of optical power density on open circuit voltage (Voc) and short circuit

current (Isc) are presented in Fig. 4.2.12(a-b), with corresponding values summarized in Table 4.2.2 for both polarization states. Fig. 4.2.12c also shows the variation of the product $I_{sc} \times V_{oc}$ with power density. These parameters (I_{sc}, V_{oc}, $I_{sc} \times V_{oc}$) increase nearly linearly with optical power density, a characteristic feature of ferroelectric materials [40] related to charge carrier generation and collection efficiency.

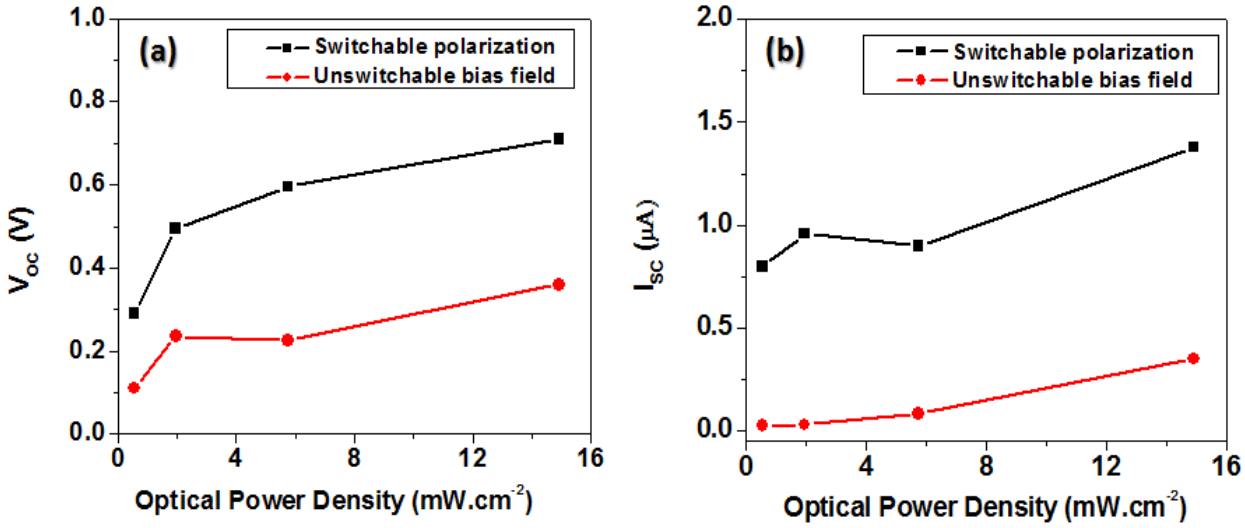

Figure 4.2.13 Variations in the switchable and un-switchable parts of **(a)** open-circuit voltage (V_{OC}) and **(b)** short-circuit current (I_{SC}) in the Ni/ZnSnS$_3$/FTO structure as a function of optical power density.

Table-4.2.2 Variation in short-circuit current (Isc) and open-circuit voltage (Voc) with changes in optical power density under illumination (λ = 532 nm) for Ni/ZnSnS$_3$/FTO devices.

Illumination intensity	Up-poled state		Down-poled state	
(mW/cm^2)	$I_{SC}(\mu A)$	$V_{OC}(V)$	$I_{SC}(\mu A)$	$V_{OC}(V)$
0.56	- 0.82	+0.18	+0.77	- 0.40
1.96	- 0.93	+ 0.26	+ 0.89	- 0.73
5.75	- 1.12	+0.37	+0.99	- 0.82
14.92	- 1.73	+0.35	+1.03	- 1.07

The photovoltaic response of the Ni/ZnSnS$_3$/FTO device under various illumination power densities can be divided into two components: the switchable open-circuit voltage (V_P^{OC}) and short-circuit current (I_P^{SC}) due to polarization, and the unswitchable components from the internal bias field (V_{bi}^{OC} *and* I_{bi}^{SC}) [41-42].

$$|V_{OC}^{P}| = \frac{1}{2}(V_{OC}^{+} - V_{OC}^{-}) \;\&\; |I_{SC}^{P}| = \frac{1}{2}(I_{SC}^{+} - I_{SC}^{-}) \qquad (3.2.9)$$

$$\left|V_{OC}^{bi}\right| = \frac{1}{2}(V_{OC}^{+} + V_{OC}^{-}) \;\&\; \left|I_{SC}^{bi}\right| = \frac{1}{2}(I_{SC}^{+} + I_{SC}^{-}) \qquad (3.2.10)$$

In the equations V_{OC}^{+}, I_{SC}^{+}, and V_{OC}^{-}, I_{SC}^{-} are parameters after positive and negative poling respectively. The resultant open-circuit voltage and short-circuit current for two components are plotted in Fig. 4.2.13. The photovoltaic response from the switchable polarization in $ZnSnS_3$ films is more significant than that from the unswitchable internal bias field, with the switchable photovoltage being roughly double. The bulk photovoltaic effect (BPVE) in $ZnSnS_3$ is complex, likely influenced by the material's non-centrosymmetric structure and a microscopic depolarization field.

Photoresponse and photodetector performance study: Figure 4.2.14a shows the temporal variation of the zero-bias photocurrent (Isc), with a magnified view in Fig. 4.2.14b. Under light illumination, the generation of electron-hole pairs increases the photocurrent [43]. A rapid rise in photocurrent is observed when the light is switched on. Conversely, after the light is turned off, the photocurrent initially drops sharply from its peak, then gradually decreases to the background level. The rise time constant (τ_r) is determined by fitting the experimental data using the following equation [43]

$$I_{Ph}(t) = I_d + A(1 - e^{\frac{t}{\tau_r}}) \tag{4.2.11}$$

The calculated response time, τ_r = 85.20 ms, suggests a fast response linked to defect-related transitions near the band gap [39], making $ZnSnS_3$ films promising for visible light photodetector applications. The decay curve was also fitted to determine recovery time constants using an empirical model with two decay channels [44].

$$I_{Ph}(t) = I_L(Ae^{-\frac{t}{\tau_{d1}}} + Be^{-\frac{t}{\tau_{d2}}}) \tag{4.2.12}$$

The values of the time constants are obtained 1.4 ms and 924.54 ms, respectively. The multiple time constants are indeed associated with the existing trap states within the band gap of the materials [43]. The noticeable photoresponse of the ZnSnS3film with sharp ON–OFF transient current characteristics under visible light suggests its suitability for self-powered detector applications in the visible range of the optical spectrum. The responsivity (R) can be measured

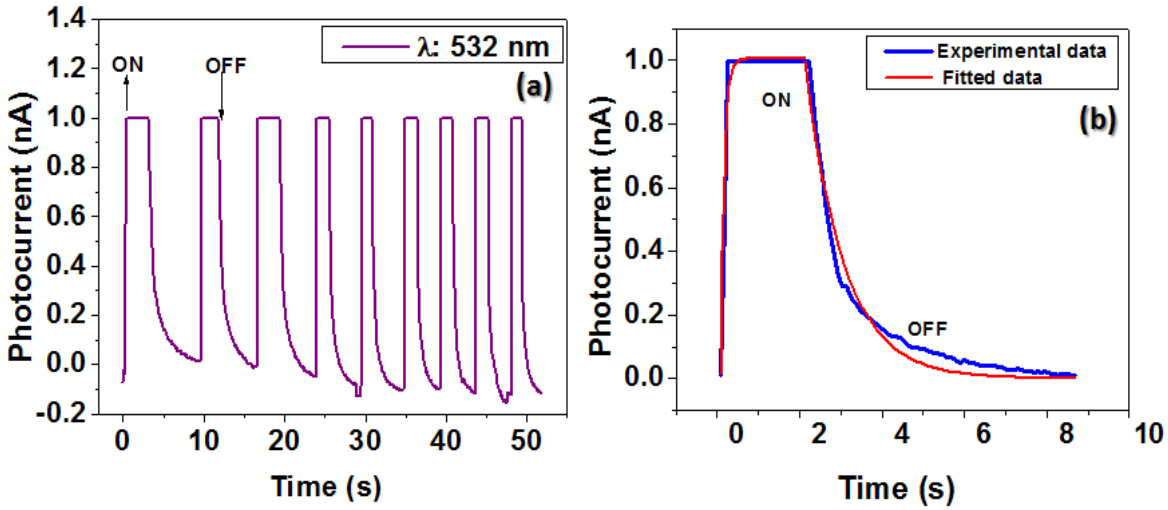

Figure 3.2.14 (a) Temporal response of zero-bias photocurrent of Ni/$ZnSnS_3$/FTO device with time with illumination ON and OFF condition **(b)** magnified view of one full cycle.

by the equation [43],

$$R = \frac{I_L - I_d}{PXA} \quad (4.2.13)$$

I_L and Id represent the total current in light and in the dark. P refers to the optical power of the incident radiation, and A is the effective illumination area (approximately 12 mm²). Under 532 nm illumination with an incident power of 5.75 mW/cm², the maximum R value at zero bias for the as grown sample was 1.45 μA/W. These results are comparable to other ferroelectric materials like BZT-BCT and $BiFeO_3$ under similar conditions [11]. Additionally, the switchable and stable photovoltaic response of the $ZnSnS_3$ film indicates its potential for data storage and logic switching applications.

5. Conclusion: We have successfully synthesized trigonal ferroelectric $ZnSnS_3$ in form of powder by hydrothermal method and in thin film form on various substrate by spray pyrolysis method. Optical, microstructural and morphological properties are examined and analysed. The ferroelectric property and its light and voltage sensitivity is observed. Also the corresponding phase transition of trigonal to monoclinic is noticed by DSC and dielectric experiment. Probable transition, recombination mechanism and defect related study is done by photoluminescence experiment. The carrier conduction mechanism as well as photovoltaic performance is studied in details after fabricating the device. Besides, the transient phenomena is studied. Based on the observed result, it is clear that the material has the potential to be a suitable candidate for solar cell, data storage, logical switching and photodetector application.

References

[1] H. Huang, Ferroelectric photovoltaics. Nat. Photonics 4, 132–135 (2010)

[2] Y. Yuan, T. J. Reece, P. Sharma, S. Poddar, S. Ducharme, A. Gruverman, Y. Yang, and J. Huang, Efficiency enhancement in organic solar cells with ferroelectric polymers. Nat. Materials 10, 296–302 (2011)

[3] S.Y. Yang, J. Seidel, S.J. Byrnes, P. Shafer, C.-H. Yang, M.D. Rossell, P. Yu, Y.-H. Chu, J.F. Scott, J.W. Ager III., L.W. Martin, R. Ramesh, Above-bandgap voltages from ferroelectric photovoltaic devices. Nat. Nanotechnol. **5**, 143–147 (2010)

[4] M. Ichiki, H. Furue, T. Kobayashi, R. Maeda, Y. Morikawa, T. Nakada, K. Nonaka, Photovoltaic properties of (Pb, La) (Zr, Ti)O_3 films with different crystallographic orientations. Appl. Phys. Lett. 87, 222903 (2005)

[5] S. Song, D. Kim, H.M. Jang, B.C. Yeo, S.S. Han, C.S. Kim, J.F. Scott, β-CuGaO2 as a strong candidate material for efficient ferroelectric photovoltaics. Chem. Mater. 29, 7596–7603 (2017)

[6] T. Choi, S. Lee, Y.J. Choi, V. Kiryukhin, S.W. Cheong, Switchable ferroelectric diode and photovoltaic effect in $BiFeO_3$. Science 324, 63–66 (2009)

[7] L. Pintilie, I. Vrejoiu, G. Le Rhun, M. Alexe, Short-circuit photocurrent in epitaxial lead zirconate-titanate thin films. J. Appl. Phys. 101, 064109 (2007)

[8] G. Zhang, H. Wu, G. Li, Q. Huang, C. Yang, F. Huang, F. Liao, J. Lin, New high *T*c multiferroics KBiFe2O5 with narrow band gap and promising photovoltaic effect. Sci. Rep. 3, 1265 (2013)

[9] X. Yang, X. Su, M. Shen, F. Zheng, Y. Xin, L. Zhang, M. Hua, Y. Chen, V.G. Harris, Enhancement of photocurrent in ferroelectric films via the incorporation of narrow bandgap nanoparticles. Adv. Mater. 24, 1202 (2012)

[10] T. Omata, H. Nagatani, I. Suzuki, M. Kita, H. Yanagi, N. Ohashi, Wurtzite CuGaO2: a new direct and narrow band gap oxide semiconductor applicable as a solar cell absorber. J. Am. Chem. Soc. 136, 3378–3381 (2014)

[11] A.B. Swain, M. Rath, P.P. Biswas, M.S. RamachandraRao, P. Murugavel, Polarization controlled photovoltaic and self-powered photodetector characteristics in Pb-free ferroelectric thin film. APL Mater. 7, 011106 (2019)

[12] G. Zhang, H. Wu, G. Li, Q. Huang, C. Yang, F. Huang, F. Liao, J. Lin, New high T_c multiferroics $KBiFe_2O_5$ with narrow band gap and promising photovoltaic effect Sci. Rep. 3 (2013) 1265.

[13] M. Qin, K. Yao, Y.C. Liang, High efficient photovoltaics in nanoscaled ferroelectric thin films. Appl. Phys. Lett. 93, 122904 (2008)

[14] Y. Liu, X. Wang, F. Fan, C. Li, The Journal of Physical Chemistry Letters 13 (2022) 11071-11075.

[15] P.F. Li, YY Tang, WQ. Liao, HY. Ye, Y. Zhang, DW. Fu, YM. You, RG Xiaong, NPG Asia mater. (2017).

[16] CP Gonzalez, G. Schileo, S. Murakami, A. Khesro, D. Wang, I.M. Reaney, A. Feteira, Appl. Phys. Lett. 110 (2017) 172902

[17] J.A. Brehm, H. Takenaka, CW. Lee, I. Grinberg, J.W. Bennett, M.R. Schoenberg, A.M. Rappe, Physical Review B. 89 (2014), 195202

[18] S. Nakashima, H. Fujisawa, S. Ichikawa, J.M. Park, T. Kanashima, M. Okuyama, M. Shimizu, Journal of Applied Physics, 108 (2010), 074106

[19] B. Kolb, A.M. Kolpak, First-principles design and analysis of an efficient, pb-free ferroelectric photovoltaic absorber derived from $ZnSnO_3$. Chem. Mater. 27, 5899–5906 (2015)

[20] R.A. Jishi, M.A. Lucas, $ZnSnS_3$: Structure Prediction, Ferroelectricity, and Solar Cell Applications, International Journal of Photoenergy, 2016, 6193502 (2016)

[21] H. Jia, M. Dirican, N. Sun, C. Chen, C. Yan, P. Zhu, X. Dong, Z. Du, H. Cheng, D. J. Guo, and X. Zhang, ChemElectroChem (2019), 6, 1183–1191.

[22] X. Liu, Y. Hao, J. Shu, H. M. K. Sari, L. Lin, H. Kou, J. Li, W. Liu, B. Yan, D. Li, J. Jhang, and X. Li, Nano Energy (2019), 57, 414–423.

[23] H. Xu, C. Wang, J. Zhang, L. Cao, B. Zhang, and X. Ou, ACS Sustain. Chem. Eng. (2020), 8, 4464–4473.

[24] R. Guo, R. Tian, D. Shi, H. Li, H. Liu, S-Doped $ZnSnO_3$ nanoparticles with narrow band gaps for photocatalytic wastewater treatment. ACS Appl. Nano Mater. 2, 7755-7765 (2019)

[25] S. Sanna, S. Neufeld, M. Rusing, G. Berth, A. Zrenner, W.G. Schmidt, Raman scattering efficiency in LiTaO3 and LiNbO3 crystals. Phys. Rev. B **91**, 224302 (2015)

[26] B. A. Nogueira, M. Rérat, R. Fausto, C. Castiglioni, R. Dovesi. Journal of Raman Spectroscopy, 53 (2022) 1904-1914

[27] M.N. Popov, J. Spitaler, V.K. Veerapandiyan, E. Bousquet, J. Hlinka, M. Deluca, Raman spectra of fine-grained materials from first principles. npj Comput. Mater. **6**, 121 (2020)

[28] X. Liu, X. Peng, T. Xu, Y. Li, H. Wei, Z. Guan, F. Wang, Broad photoluminescence in ternary Ag-In-S and quaternary Ag-In-Zn-S nanoparticles: the role of Zn incorporation, Mater. Res. Express. 8 (2021) 085002

[29] D. M. Eagles, Optical absorption and recombination radiation in semiconductors due to transitions between hydrogen-like acceptor impurity levels and the conduction band, J. Phys. Chem. Solids. 16 (1960) 76-83.

[30] S. Mukherjee, T. Maitra, A. Nayak, S. Mukherjee, A. Pradhan, M. K. Mukhopadhyay, B. Satpati, S. Bhunia, Microstructural and light emission properties of $ZnSnP_2$ thin film absorber: Study of native defects, Mater. Chem. Phys. 204 (2018) 147-153

[31] C. Spindler, T. Galvani, L. Wirtz, G. Rey, S. Siebentritt, Excitation-intensity dependence of shallow and deep-level photoluminescence transitions in semiconductors, J. Appl. Phys. 126 (2019) 17570

[32] X.-Y. Chen, J.-Q. Tan, K.-R. Su, J.-H. Yang, X.-F. Xu, G.-P. Luo, W.-L. Zhu, S.-M. Hu, G.-X. Lai, H. Ji, L.-T. Niu, First-principles study of R3c-MgSnX3 (X=O, S and Se) for photovoltaic and ferroelectric application. Phys. Lett. A **422**, 127774 (2022)

[33] B. Ofuonye, J. Lee, M. Yan, C. Sun, J.M. Juo, I. Ilesanmi, Electrical and microstructural properties of thermally annealed Ni/Au and Ni/Pt/Au Schottky contacts on AlGaN/GaN heterostructures. Semicond. Sci. Technol. **29**, 095005–095015 (2014)

[34] M.G. Helander, M.T. Greiner, Z.B. Wang, W.M. Tang, Work function of fluorine-doped tin oxide. J. Vac. Sci. Technol. A **29**, 011019 (2011)

[35] L.A. Burton, T.J. Whittles, D. Hesp, W.M. Linhart, J.M. Skelton, B. Hou, R.F. Webster, G. O'Dowd, C. Reece, D. Cherns, D.J. Fermin, T.D. Veal, V.R. Dhanak, A. Walsh, Electronic and optical properties of single crystal SnS2: an earth-abundant disulfide photocatalyst. J. Mater. Chem. A **4**, 1312–1318 (2016)

[36] Y. Yang, S. Xue, S. Liu, J. Huang, J. Shen, Fabrication and characteristics of ZnS nanocrystals/polymer composite doped with tetraphenylbenzidine single layer structure light-emitting diode. Appl. Phys. Lett. **69**, 377–379 (1996)

[37] L. Huang, M. Wei, C. Gui, L. Jia, Ferroelectric photovoltaic effect and resistive switching behavior modulated by ferroelectric/electrode interface coupling. Journal of Materials Science: Materials in Electronics (2020).

[38] R.R. Mehta, B.D. Silverman, J.T. Jacobs, Depolarization fields in thin ferroelectric films. J. Appl. Phys. **44**, 3379– 3385 (1973)

[39] D. Lee, S.H. Baek, T.H. Kim, J.G. Yoon, C.M. Folkman, C.B. Eom, T.W. Noh, Polarity control of carrier injection at ferroelectric/metal interfaces for electrically switchable diode and photovoltaic effects. Phys. Rev. B **84**, 125305 (2011)

[40] Y. Yuan, Z. Xiao, B. Yang, J. Huang, Arising applications of ferroelectric materials in photovoltaic devices. J. Mater. Chem. A **2**, 6027–6041 (2014)

[41] W. Ji, K. Yao, Y.C. Liang, Bulk photovoltaic effect at visiblen wavelength in epitaxial ferroelectric BiFeO3 thin films. Adv. Mater. **22**, 1763–1766 (2010).

[42] K. Mistewicz, M. Nowak, D. Stroz, Ferroelectric-photovoltaic effect in SbSi nanowires. Nanomaterials **9**, 580 (2019).

[43] S. Mukherjee, T. Maitra, A. Pradhan, S. Mukherjee, G. Manna, S. Bhunia, A. Nayak, Rapid responsive Mg/$ZnSnP_2$/Sn photodetector for visible to near-infrared application. Sol. Energy Mater. Sol. Cells **189**, 181–187 (2019)

[44] S. Mukherjee, T. Maitra, A. Pradhan, S. Bhunia, A. Nayak Probing bias and power dependency of high-performance broadband Mg/$ZnSnP_2$/Sn back-to-back Schottky junction photodetectors. Solar Energy Materials and Solar Cells, 208 (2019)

Publication related to my thesis

1. **Md. Mohsin**, S. Bhunia, A. Nayak, Ferroelectric $ZnSnS_3$ thin films: growth and measurement of photovoltaic properties, J. Mater. Sci: Mater Electron 34 (2023) 2194, https://doi.org/10.1007/s10854-023-11545-w

2. **Md. Mohsin,** J. Sharma, G. Ghorai, P. K. Sahoo, S. Bhunia, A. Nayak, Characterization of polycrystalline bulk ferroelectric $ZnSnS_3$ synthesized by hydrothermal method for photovoltaic application, Materials Today Communications 41 (2024) 110387, doi.org/10.1016/j.mtcomm.2024.110387

Conferences attended (poster presented)

1. ***International Conference on Advance Physics: IEMPHYS-22***

Title of the poster: Microstructural and optical properties of ferroelectric $ZnSnS_3$ films grown by spray pyrolysis method, **Md. Mohsin**, S. Bhunia and A. Nayak

2. ***7th International Conference on Nanoscience and Nanotechnology: ICONN-2023***

Title of the poster: Electrical behaviors of ferroelectric $ZnSnS_3$ thin films synthesized by spray pyrolysis method for photovoltaic applications, **Md. Mohsin**, Ishita Ghose, Satyaban Bhunia and Arabinda Nayak

3. ***National Conference on "Physics of Nano Devices and Quantum Materials: Harnessing The Power of Small": PNDQM-2024***

Title of the poster: Microstructural and optical characteristics of polycrystalline ferroelectric $ZnSnS_3$ powder synthesized by hydrothermal method for photovoltaic applications, **Md. Mohsin**, Satyaban Bhunia and Arabinda Nayak